Modelling of cyclic visco-elasto-plastic behaviour of coated woven fabrics under biaxial loading and finite strain

W. Dib, Guilhem Blès, A. Blaise, A. Tourabi

Modelling of cyclic visco-elasto-plastic behaviour of coated woven fabrics under biaxial loading and finite strain

W.Dib[1], G.Bles[2], A.Blaise[1]and A.Tourabi[1]

[1]Grenoble-INP, UJF-Grenoble 1, CNRS UMR 5521, 3SR Lab, Grenoble F-38041, France,

Ali.Tourabi@3sr-grenoble.fr, www.3sr-grenoble.fr

[2] ENSTA Bretagne, FRE CNRS 3744, IRDL, Brest F-29200, France,

Guilhem.Bles@ensta-bretagne.fr, www.irdl.fr

Abstract

This paper deals with the modelling of the mechanical behaviour of coated woven fabric. The proposed model takes into account the individual behaviours of the yarns, the coating and their interactions including the influence of the angle variation between warp and weft yarns. This model is able to describe simultaneously the non-Newtonian viscous behaviour, the time-independent irreversibility, the anisotropy and the cyclic loading behaviour. The model was implemented in the finite element code ABAQUS and enables calculations on structures such as complete sails.

Keywords: *Behaviour of sailcloth materials, Synthetic fibres, Textile, finite deformation, viscous effects, anisotropy, cyclic loading*

1. Introduction

The study focuses on the modelling of mechanical behaviour of woven materials with an additional coating. For example, woven fabrics can be based on synthetic filament fibres such as polyester (Dacron^{TM}), polyamide (Nylon^{TM}), aramid (Kevlar^{TM}), high modulus polyethylene UHMWPE (Dyneema^{TM}, Spectra^{TM}), liquid crystal aromatic polyester (Vectran^{TM}) or glass fibres. From a design aspect, those materials offer a multitude of possibilities in terms of the resulting behaviour of the final material. The polyamide- and polyester-fibres woven fabrics are now the most spread materials in the construction of cruise ships sails (mainsail, spinnaker). PTFE-coated glass-fibres and PVC-coated polyester woven fabrics are used for tensioned membrane or fabric structures (TFS) as light-weight roof structures (see Bridgensand Gosling (2004)). Other applications of coated woven fabric include geotextiles (see Horrocks and Anand (2000)), stratospheric airship envelopes (see Chen et al. (2014)), as well as inflatable structures and safety equipment (belts, airbags...) (see Oñate and Kröplin (2008)). Moreover, these materials are currently the most adequate for the production of giant kites for auxiliary ship propulsion in order to reduce their fuel consumption (see for instance, Leloup et al. (2013a), (2013b), (2014), (2016)).

Several major arguments motivate our contribution: (i) The aerodynamic profile of sails is closely related to their deformation under the effect of repeated cyclic loading. The performance evaluation of sails and the study of the fluid-structure interactions with wind require detailed modelling of the behaviour of these fabric structures (see for instance, Le Maitre et al. (1998), Bessert and Frederich (2005), Graf and Renzsch (2006), Ciortan and Guedes Soares (2007), Lasher and Sonnenmeier (2008)). This point concerns also the kites (see Leloup et al. (2013a)) and the tensioned fabric structures (see Lewis (2003)). (ii) Applications like giant kite design for auxiliary ship propulsion raise problems related to the mechanical performance of the materials and the need to have available efficient tools to support the design. Indeed, if we switch from a conventional kite (typically $10m^2$) to a giant

kite (typically 1000m^2) (scale ratio: k), aerodynamic forces that are proportional to the surface evolve according to k^2, while the weight evolves according to k^3 (see Bles et al. (2012)). Thus, switching to large size kite will increase the weight to aerodynamic lift ratio, reducing its ability to float in the air. If now we consider a typical mass per unit area of the material, with a low thickness in order to promote the ability to fly and to reduce the weight of the structure, operating stress drastically increases in the material. Thus, they reach stress levels far beyond the stress limits that are generally accepted for this kind of application concerning typical materials like polyamide and polyester. (iii) The mechanical behaviour of coated woven fabric is the result of the behaviours of all its components; the fibres, the weave or interactions between warp and weft and the coating. For example, in the case of the shape of sails, of kites and of architectural tensioned membrane structures, the structural behaviour under operating conditions and also anisotropy are closely linked to the choice of fibres orientations (and of the coating). Indeed, the fibres as well as the coating have a non-linear elastic behaviour with a mechanical non-Newtonian viscous contribution and a time-independent irreversible behaviour, which is not negligible (Dib (2014)). Thus, predicting the behaviour of a filamentary membrane, according to the choice of its design, is a complex problem, which is a scientific hindrance for the development of these materials and needs a better understanding of the behaviour of the components and, more importantly, of their effect on the coated woven material behaviour. A validated modelling approach of a mechanical behaviour is generally a great step towards the understanding of the involved mechanical phenomena. In order to understand the effect of the components behaviours and their interactions, the modelling approach should take into account these components and how they are coupled.

Prior research works put forward woven reinforced stiff composite materials (Tabiei and Jiang (1999), Tabiei and Yi (2002)), especially in order to predict the rupture or the anisotropic elastic moduli. But the matrix stiffness of these materials implies a behaviour that

is different compared to the coated woven fabric whose coating is more flexible. Concerning the coated woven fabrics, Chen and Ding (2007), tested a PVC-coated polyester woven fabrics in traction in different directions and proposed a linear orthotropic elastic model in order to identify the elastic moduli from those tensile tests. But, the coated woven fabric may undergo important strains in case of shear loading or in tensile loading in a direction of 45° from warp and weft directions. Thus, the angle between warp and weft directions might vary greatly. The linear anisotropic elastic models remain no longer relevant because they do not take into account those angle variations. Xue et al. (2003), Peng and Cao (2005) proposed linear anisotropic elastic models that can follow the warp and weft direction in high strain levels. They could implement their model in the finite element code Abaqus. To go further in the description of the coated woven fabrics behaviour, Kato et al. (1999) put forward a simple model of entanglement and interaction of the weaving warp and weft fibres. This enables the description of the crimp phenomena but also to define their fabric behaviour from the one of their components (yarns, coating). Their behaviour model is non-linear and anisotropic and takes into account the hysteresis observed during biaxial tests composed of a loading and followed by an unloading. Furthermore, Pargana et al. (2007) and Pargana and Leitao (2015) proposed a similar model that they could implement in a membrane finite element in order to simulate tensioned fabric structures. King et al. (2005) also propose another similar model based on the yarns and the weaving properties for a Kevlar-fibre woven fabric that they implemented in Abaqus. Instead of modelling the weaving by an analytical model, other authors, like Badel et al. (2007) modelled by finite elements, the yarns entanglement network of a weaving. This created difficulties in the numerical calculation but brought further information about contacts between the yarns, and about efforts and strain in the yarns section for example. But this modelling method cannot be used directly for the calculation of a membrane structure in coated woven fabric, because of the too large number of degrees of

freedom that are necessary for a representative element volume (R.E.V.) of the weaving. Other non-linear anisotropic elastic behaviour laws have been proposed for coated woven fabric (see for instance Bridgens and Gosling (2004), Minami (2006)). Those are phenomenological models. They are defined by linear or non-linear multivariable analytical functions. The parameters involved in these functions were identified from the results of biaxial mechanical tests. Minami (2006) could implement his model in a finite element code in order to simulate PTFE-coated woven-glass-fibre fabrics for architectural membrane structures. Ambroziak (2006) and also Galliot and Luchsinger (2009) proposed a non-linear anisotropic elastic models for coated woven fabric. Galliot and Luchsinger (2009) observed a linear relationship between elastic moduli and a tension ratio for numerous PVC-coated polyester fabrics. Their model also has been implemented in a finite element code. Dinh et al. (2014) proposed a non-linear anisotropic elasto-plastic model for PVC coated polyester fabric. Their elasto-plastic behaviour law is simple but can model a strain ratcheting phenomenon during cyclic loading, i.e. increasing strain when stress carries out cycles between two constant values. The parameters of their model have been identified and this latter has been implemented into the finite element code Abaqus in order to simulate tension membrane structures. Those works did not broach the subject of viscosity. The viscosity of a PVC-coated polyester woven fabric has been the object of a modelling work by Klosowski et al. (2009) from a dense net model of two fibres families. The warp and weft tensions depends (in a decoupled manner) on the warp and weft strains respectively. The behaviour law in the yarns is of Schapery viscoelastic type. The identification of the model has been performed on the basis of creep tests in the yarn's direction. The cyclic behaviour was not the object of this study.

Thus, to our knowledge, few studies in the literature dealt with the simultaneous modelling of the viscous behaviour, the time-independent irreversibility, the anisotropy and

the cyclic loading behaviour of coated woven fabric. The originality of the model put forward in this paper lies in the consideration of all those aspects in the case of woven materials provided with a coating. For the fine prediction of the behaviour of sails, kites and other structures, the model takes into account the individual behaviours of the coating, the fibres and also the interaction between the fibres at binding points. The model also takes into account the angle variation between warp and weft fibres. The implementation of the model was made in a commercial finite element code (Abaqus) in order to produce an operational tool that allows numerical calculation to predict the structural behaviour of complex structures of coated woven fabrics under operating conditions and in terms of performance. This implementation was carried out in the membrane case. Therefore, the proposed model focuses on behavior in the plane tangent to the surface of the membrane and does not address the wrinkles phenomenon.

This paper contains the following main parts: The part 2 gathers all the hypotheses adopted in the modelling of woven materials. The parts 3 and 4 describe respectively, the 1D (scalar) and the 2D (tensorial) constitutive models for describing the behaviour of fibres and coating. The part 5 develops the exploitation and assessment of the constitutive model. In this part, is given: (i) an identification method of the model; (ii) the confrontation of the model according to experimental results obtained with a woven polyester material provided with a coating; (iii) the results of the implementation of the model in the finite elements code Abaqus in the case of calculation of a whole sail under operating conditions.

2. Modelling hypotheses

The notations and symbols used in the following are summed up in the Table 1.

Symbol	Definition
	Scalar
$\vec{a}$	Vector
	Tensor
	Transpose of a tensor
	Tensor $\left(\mathbf{A} \quad\right)$ or $\left(\mathbf{A}^{\mathrm{T}}\right)$
$\overline{\mathbf{A}}$	Deviatoric tensor
$\underline{\vec{A}}$	Vector that stands for a deviatoric tensor
$\|\|\vec{a}\|\|$	Norm of a vector
	Tensorial product

Table 1. Notations and symbols

2.1. Preliminary

The applications covered in this work relate to coated woven fabrics for the manufacture of sails. In these applications, the materials have very low thickness compared to the size of the sail and the typical radius of curvature of these structures. Besides, the shape of the sail is essentially linked to its rigidity and its surface deformation. The bending stiffness is relatively low and shear within thickness has negligible effect on the overall shape of the sail. The woven material will be described as a membrane and not as a shell. This assumption is equivalent to consider the material as a two-dimensional membrane (2D) and to neglect stress and strain in the thickness. Then, the material has no bending and shear stiffness in the thickness, which implies a plane stress hypothesis, in relation to the axis perpendicular to the

membrane plane. This assumption on the stress is completed by a kinematic hypothesis, which consists of neglecting the contraction effect in the thickness, implying the consideration of a null Poisson ratio in the thickness of the membrane. Thus, stress and strain tensors are tensors in the two-dimensional vector space (2D) corresponding to the plane tangent to the surface of the membrane. This hypothesis limits the scope of the model which does not address the modeling of the wrinkles phenomenon for which it is necessary to introduce the material bending stiffness. Furthermore, the constituting yarns of woven material or canvas are considered as a one-dimensional material (1D), which has no torsional and bending stiffness. The yarns do not show any longitudinal nor transverse shearing effect. The only components of the stress and strain are those along the yarn axis.

The model proposed in this work relates to a family of coated woven materials with one direction of the yarns that is straight and the other one that is crimped. According to the considered weaving process, the crimp phenomenon essentially affects the warp direction; while the weft direction, which is stretched during the process, remains relatively straight and very little affected by the crimp phenomenon. The experimental results of simple tensile tests in the warp and weft directions show that the lateral effect of contraction is much more important in the case of tensile in weft direction. At the mesoscopic level and according to the weaving, the weft yarns are straight and the warp yarns oscillate around the weft yarns and have a crimp. Thus, the straight shape of the weft yarns gives them better compressive strength and reduces the lateral effect during warp tensile. Unlike the weft yarn, the warp yarns naturally have a better compressive deformation ability, which favours the contraction effect, during tensile test in the weft direction. To model this behaviour, it results from this analysis that it is necessary to adopt non-zero compression stiffness for a straight yarn. The experimental characterization of this compression stiffness remains difficult, if not impossible,

by a direct measurement. Nevertheless, the comparison of contraction measurements in warp and weft directions enables us to access to this characterization.

2.2. Membrane hypothesis

The membrane is a surface defined by two curvilinear coordinates φ^1 and φ^2 that enable to locate a material point P. At any time, there is an injective relation of class $\mathcal{C}^1$ of the material coordinates $\varphi^1$and $\varphi^2$to the spatial coordinates $\vec{x} = \vec{x}(\varphi^1, \varphi^2)$ (Fig. 1-a). For a given material point P, the material coordinates φ^i $(i = 1,2)$ have a fixed given values throughout time. An infinitesimal variation $d\varphi^i$ corresponds to a variation of the point P and consequently to a variation $d\vec{x}$ of the position vector in the current configuration. We define the following vectors:

$$\vec{g}_1 = \frac{\partial \vec{x}}{\partial \varphi^1} \quad ; \quad \vec{g}_2 = \frac{\partial \vec{x}}{\partial \varphi^2} \quad \text{and} \quad \vec{g}_3 = \frac{\vec{g}_1 \wedge \vec{g}_2}{\|\vec{g}_1 \wedge \vec{g}_2\|} \qquad (1)$$

where the vector $\vec{g}_i$ is the tangent to the curve φ^i $(i = 1,2)$ and $\vec{g}_3$ is an unit vector normal to the membrane plane at P; $(\vec{g}_1, \vec{g}_2, \vec{g}_3)$is a covariant natural basis in the current configuration. We introduce the dual basis or contravariant natural basis $(\vec{g}^1, \vec{g}^2, \vec{g}^3)$, in the current configuration, such as:

$$\vec{g}^i . \vec{g}_j = \delta^i{}_j \quad , \quad (i, j = 1,2,3) \qquad (2)$$

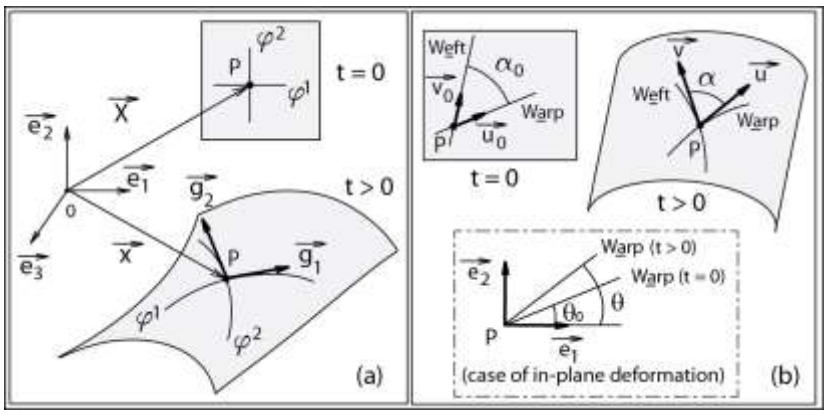

Fig. 1. Membrane hypothesis: (a) Curvilinear coordinates, (b) Normed natural covariant basis$(\vec{u}, \vec{v})$.

In the current configuration, the infinitesimal vector in the tangent plane $d\vec{x}$ can be written:

$$d\vec{x} = \underset{\sim}{\mathbf{F}}.d\vec{X} \qquad (3)$$

where $\underset{\sim}{\mathbf{F}}$ is the transformation gradient tensor of the membrane and $\mathrm{d}\vec{\mathrm{X}}$ the elementary vector in the initial configuration, $\underset{\sim}{\mathbf{F}}$ is an order 2 tensor defined such as :

$$\underset{\sim}{\mathbf{F}} = \sum_{i=1}^{3}\left(\vec{g}_i \otimes \vec{G}^i\right) \qquad (4)$$

where, $(\vec{G}^1, \vec{G}^2, \vec{G}^3)$ is the contravariant natural basis in the initial configuration. Consequently,

$$\vec{g}_i = \underset{\sim}{\mathbf{F}}.\vec{G}_i \quad \text{and} \quad \vec{g}^i = \underset{\sim}{\mathbf{F}}^{-\mathrm{T}}.\vec{G}^i \quad \text{with (i=1,2,3)} \qquad (5)$$

This expression reflects the convective transport, by the transformation of the natural basis vectors starting from the initial configuration to the current configuration. The 2D identity tensor or metric tensor $\underset{\sim}{\mathbf{I}}$, in the current tangent plane, is such as:

$$\begin{aligned} \underset{\sim}{\mathbf{I}} &= \sum_{i=1}^{2}\left(\vec{g}_i \otimes \vec{g}^i\right) = \sum_{i=1}^{2}\left(\vec{g}^i \otimes \vec{g}_i\right) \\ \underset{\sim}{\mathbf{I}} &= \sum_{i,j=1}^{2}\left(g^{ij}\vec{g}_i \otimes \vec{g}_j\right) = \sum_{i,j=1}^{2}\left(g_{ij}\vec{g}^i \otimes \vec{g}^j\right) \end{aligned} \qquad (6)$$

where the covariant and contravariant components are given by :

$$g_{ij} = \vec{g}_i.\vec{g}_j \quad ; \quad g^{ij} = \vec{g}^i.\vec{g}^j \quad (i,j = 1,2) \text{ and } \quad \sum_{k=1}^{2}\left(g^{ik}.g_{kj}\right) = \delta^i{}_j \qquad (7)$$

The vectors of the natural basis can be expressed in the dual basis and reciprocally by the following relations:

$$\vec{g}_i = \sum_{j=1}^{2}\left(g_{ij}.\vec{g}^j\right) \quad ; \quad \vec{g}^i = \sum_{j=1}^{2}\left(g^{ij}.\vec{g}_j\right) \quad , (i = 1,2) \qquad (8)$$

The covariant components g_{ij} and contravariant components g^{ij} of the metric tensor can be calculated as follows:

$$g_{ij} = \vec{G}_i.\left(\underset{\sim}{\mathbf{F}}^T\,\underset{\sim}{\mathbf{F}}\right).\vec{G}_j \quad \text{and} \quad g^{ij} = \vec{G}^i.\left(\underset{\sim}{\mathbf{F}}^{-1}\underset{\sim}{\mathbf{F}}^{-T}\right).\vec{G}^j \quad , (i,j = 1,2) \qquad (9)$$

In the case of a woven material, the material coordinated φ^1 and φ^2 are chosen respectively along the warp yarns and along the weft yarns. The angle between the warp yarns and the weft yarns, at a point P of the woven material is written α_0 in the initial configuration and α in the current configuration.The initial value of angle between warp and weft yarns α_0 may be different of $\frac{\pi}{2}$.We note the normed natural covariant basis and the normed dual basis, respectively $(\vec{u}, \vec{v})$and $(\vec{u}^*, \vec{v}^*)$, in the current configuration and $(\vec{u}_0, \vec{v}_0)$ and $(\vec{u}_0^*, \vec{v}_0^*)$ in the initial configuration (Fig.1-b), such as :

$$\begin{cases} \vec{u} = \frac{\vec{g}_1}{\sqrt{g_{11}}} \; ; \; \vec{u}^* = \frac{\vec{g}^1}{\sqrt{g^{11}}} \\ \vec{v} = \frac{\vec{g}_2}{\sqrt{g_{22}}} \; ; \; \vec{v}^* = \frac{\vec{g}^2}{\sqrt{g^{22}}} \end{cases} \quad \text{et} \quad \begin{cases} \vec{u}_0 = \frac{\vec{G}_1}{\sqrt{G_{11}}} \; ; \; \vec{u}_0^* = \frac{\vec{G}^1}{\sqrt{G^{11}}} \\ \vec{v}_0 = \frac{\vec{G}_2}{\sqrt{G_{22}}} \; ; \; \vec{v}_0^* = \frac{\vec{G}^2}{\sqrt{G^{22}}} \end{cases} \qquad (10)$$

The warp direction is oriented by the angles θ_0 and θ, respectively in the initial configuration $(t = 0)$ and in the current configuration $(t > 0)$ (Fig.1-b).

2.3. Deformation of woven fabric

The variation of the surface between the reference and the current configuration, is defined by the Jacobian J of the transformation, such as :

$$J = \frac{ds}{dS} = \det(\underset{\sim}{\mathbf{F}}) = \lambda_1 \lambda_2 \qquad (11)$$

Where $\lambda_1$and $\lambda_2$are the membrane elongations or eigenvalues of $\underset{\sim}{\mathbf{V}}$ the left pure strain tensor. In order to characterize the deformation of a woven material, we use the left Hencky tensor $\underset{\sim}{\boldsymbol{\varepsilon}}$, also called Eulerian logarithmic strain tensor, such as :

$$\underset{\sim}{\boldsymbol{\varepsilon}} = ln\left(\underset{\sim}{\mathbf{V}}\right) \qquad (12)$$

The eigenvalues of the tensor $\underset{\sim}{\boldsymbol{\varepsilon}}$ can be expressed as a function of the elongations, such as:

$$\varepsilon_i = ln(\lambda_i) \qquad \text{(i=1,2)} \qquad (13)$$

Other strain parameters can be defined to characterize the local deformation of the woven material in the w**a**rp direction and in the w**e**ft direction such as, respectively,

$$\varepsilon_a = ln\left(\frac{\sqrt{g_{11}}}{\sqrt{G_{11}}}\right) \qquad \text{and} \qquad \varepsilon_e = ln\left(\frac{\sqrt{g_{22}}}{\sqrt{G_{22}}}\right) \qquad (14)$$

We also define a distortion angle γ of the woven material such as :

$$\gamma + \alpha = \frac{\pi}{2} \qquad (15)$$

To this distortion angle, we assign a distortion strain, denoted ε_γ such as:

$$\varepsilon_\gamma = \frac{1}{2}(\gamma - \gamma_0) = \frac{1}{2}\{arcsin(\vec{u}\,.\,\vec{v}) - arcsin(\vec{u}_0\,.\,\vec{v}_0)\} \qquad (15)$$

where, γ_0 is the angle defined in the initial configuration such as :

$$\gamma_0 + \alpha_0 = \frac{\pi}{2} \qquad (16)$$

2.4. Notion of specific stress

The definition and the measurement of the cross section of woven material is a difficult operation. This problem is raised experimentally as well as theoretically, whether the material is 1D (ropes, straps) or 2D (woven materials). This difficulty comes from the fact that the nature of woven materials is not a continuous medium. Indeed, this latter can be rather seen as a structure composed of different layers, of voids, of different kind of yarns, of coatings etc. It means that the apparent geometrical cross section of a woven material cannot be a good parameter for the stress definition. In fact, it is not the geometric surface, but rather the material itself that transmits the forces. In that case, the mass may be an alternative to the geometric section to qualify and quantify the material undergoing mechanical actions. Consequently, instead of the Cauchy stress tensor, we rather use the specific stress tensor $\underset{\sim}{\boldsymbol{\Sigma}}$

defined as the ratio between the Cauchy stress tensor $\boldsymbol{\sigma}$ and the mass per unit volume ρ^t of the current material:

$$-\qquad (17)$$

This definition has been already used by other authors such as: Alfthan, J. (2004), Bele et al. (2009), Curnier (2005), Fitzgerald (2008), FER (1971), Leclère et al. (2004), Mandel (1974) and Rougée (1997). The current mass per unit volume can be written as:

$$\underline{\bar{\rho}^t} \qquad (18)$$

where $\bar{\rho}^t$ and e are respectively the current mass per unit surface and the current thickness of the woven material. Consequently, the definition of the specific stress can be written as follows:

$$\overline{\bar{\rho}^t} \qquad (19)$$

To illustrate the advantage of the use of the specific stress notion, let us consider the case of an orthotropic woven material which undergoes a homogeneous deformation during a simple tensile test along its warp or weft axes. Figure 2 stands for a sample of initial dimensions (L, H, E) and current dimensions (l, h, e). The initial cross section is The current cross section that is e, undergoes a tensile force $\overrightarrow{f_1}$. The axial elongation under traction is –, the transverse elongation is – and the elongation in the thickness is –. In that case, the Jacobian is:

$$\left(\boldsymbol{F}\right) \qquad - \qquad \frac{\bar{\rho}}{\bar{\rho}^t} \qquad (20)$$

which leads to:

$$\bar{\rho} \qquad \underline{\bar{\rho}} \qquad (21)$$

where ρ is the initial mass per unit volume and $\bar{\rho}$ the initial mass per unit surface. Besides, the axial component of the Cauchy stress for a simple tensile test, called σ_1 can be written such as :

$$\sigma_1 = \frac{f_1}{a} = \frac{f_1}{A\,\lambda_2\,\lambda_3} \qquad (22)$$

where f_1 stands for the intensity of the tensile force $\vec{f}_1$.

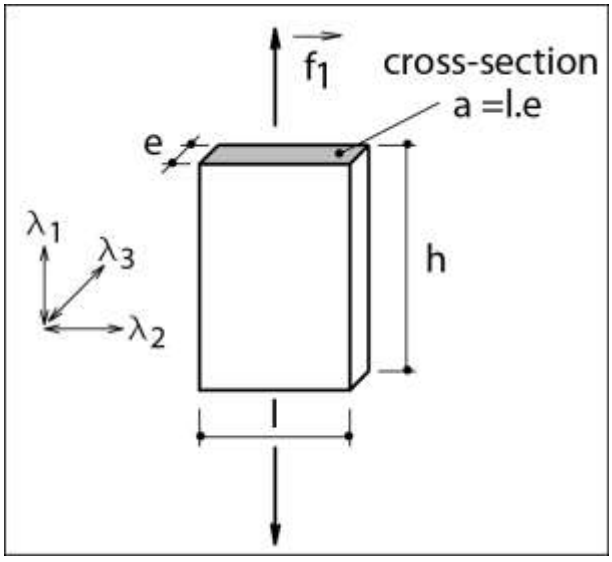

Fig.2. Simple tensile test of a woven material sample.

According to Eq. (17) to Eq.(22), the axial component of the specific stress in a simple tensile test, called Σ_1 can be written as follows:

$$\Sigma_1 = \frac{\lambda_1}{\bar{\rho}}.\frac{f_1}{L} \qquad (23)$$

Thus, the axial specific stress applied to the sample is calculated from the applied axial force f_1, the axial elongation λ_1, the initial mass par unit surface $\bar{\rho}$, and the initial width L of the sample. This definition of the specific stress puts forward an advantage to the experimental point of view. Indeed, it enables a rigorous definition of stress without involving the cross section measurement, that remains quite difficult in the case of woven materials,

contrary to the Cauchy stress that requires the measurement of the initial section A of the sample and the elongations λ_2 and λ_3. Eq.(17) shows that the specific stress unit measure is the Newton.meter per kilogram $\left[\frac{N.m}{kg}\right]$ or the Joule per kilogram $\left[\frac{J}{kg}\right]$.

2.5. Fundamental hypothesis of stress superimposition

The hypothesis presented here is a fundamental hypothesis resulting from a physical analysis at the mesoscopic scale. The woven material under consideration can be seen as the merging of two layers constituted by yarns in w**a**rp and w**e**ft directions and an additional **c**oating layer. This is illustrated by Fig.3. All the layers have the same fictitious thickness e^* that corresponds with the thickness e of the final material. According to the weaving nature of the material, an **i**nteraction is considered between the both yarns layers. The superimposition hypothesis concerns the specific stress in each layer. At the mesoscopic scale, around a point P, a surface element ds is loaded by a specific stress state $\underset{\sim}{\boldsymbol{\Sigma}}$ that can be considered as the sum of four contributions, such as:

$$\underset{\sim}{\boldsymbol{\Sigma}} = \frac{\overline{\rho}_a}{\overline{\rho}}.\ \underset{\sim}{\boldsymbol{\Sigma_a}} + \frac{\overline{\rho}_e}{\overline{\rho}}.\ \underset{\sim}{\boldsymbol{\Sigma_e}} + \frac{\overline{\rho}_f}{\overline{\rho}}.\ \underset{\sim}{\boldsymbol{\Sigma_i}} + \frac{\overline{\rho}_c}{\overline{\rho}}.\ \underset{\sim}{\boldsymbol{\Sigma_c}} \qquad (24)$$

where $\underset{\sim}{\boldsymbol{\Sigma_a}}$, $\underset{\sim}{\boldsymbol{\Sigma_e}}$,$\underset{\sim}{\boldsymbol{\Sigma_c}}$ and $\overline{\rho}_a, \overline{\rho}_e, \overline{\rho}_c$ denote respectively specific stress and initial mass per unit surface in the three layers: w**a**rp, w**e**ft and **c**oating. The **i**nteraction between yarns layers, that takes part at binding points, is characterized by a specific stress $\underset{\sim}{\boldsymbol{\Sigma_i}}$ and by initial mass per unit surface $\overline{\rho}_f$, which corresponds to the sum of the initial masses per unit surface taking part in the interaction, i.e. $\overline{\rho}_f = \overline{\rho}_a + \overline{\rho}_e$. The initial mass per unit surface of the whole material is $\overline{\rho} = \overline{\rho}_a + \overline{\rho}_e + \overline{\rho}_c$.We complete this hypothesis by an assumption whereby all the layers undergo the same deformation, such as:

$$\underset{\sim}{\mathbf{F}} = \underset{\sim}{\mathbf{F_a}} = \underset{\sim}{\mathbf{F_e}} = \underset{\sim}{\mathbf{F_c}} \qquad (25)$$

where $\underset{\sim}{\mathbf{F}}$, $\underset{\sim}{\mathbf{F_a}}$, $\underset{\sim}{\mathbf{F_e}}$ and $\underset{\sim}{\mathbf{F_c}}$ are the transformation gradient tensors, respectively of the final material, of the w**a**rp yarns layer, of the w**e**ft yarns layer and of the **c**oating layer.

Equations (24) and (25) are fundamental assumptions that lie at the heart of our proposal. The theoretical approach, which results from those both hypotheses, has a phenomenological nature. It considers the woven material as a continuous material endowed with particular properties, linked to behaviour of the different constitutive layers and their interactions.

Considering the normed natural covariant basis and the normed dual basis, respectively $(\vec{u}, \vec{v})$and $(\vec{u}^*, \vec{v}^*)$, defined by Eq.(10), the total specific stress of Eq.(24), can be written:

$$\underset{\sim}{\boldsymbol{\Sigma}} = \frac{\overline{\rho}_a}{\overline{\rho}} \Sigma_a(\vec{u} \otimes \vec{u}) + \frac{\overline{\rho}_e}{\overline{\rho}} \Sigma_e(\vec{v} \otimes \vec{v}) + \frac{\overline{\rho}_f}{\overline{\rho}} \Sigma_i(\vec{u}^* \otimes \vec{v} + \vec{v}^* \otimes \vec{u}) + \frac{\overline{\rho}_c}{\overline{\rho}} \underset{\sim}{\boldsymbol{\Sigma}_c} \qquad (26)$$

Where$(\vec{u} \otimes \vec{u})$, $(\vec{v} \otimes \vec{v})$and $(\vec{u}^* \otimes \vec{v} + \vec{v}^* \otimes \vec{u})$are three symmetric tensors;Σ_a, Σ_e and Σ_i are three scalar components of specific stresses; $\underset{\sim}{\boldsymbol{\Sigma}_c}$ is a symmetric tensor. The tensor $\underset{\sim}{\boldsymbol{\Sigma}_c}$ can be decomposed into an isotropic part $\Sigma_c \underset{\sim}{\mathbf{I}}$ and a deviatoric part $\underset{\sim}{\overline{\boldsymbol{\Sigma}}_c}$ such as:

$$\underset{\sim}{\boldsymbol{\Sigma}_c} = \Sigma_c \underset{\sim}{\mathbf{I}} + \underset{\sim}{\overline{\boldsymbol{\Sigma}}_c} \qquad \text{and} \qquad \Sigma_c = \frac{tr(\underset{\sim}{\boldsymbol{\Sigma}_c})}{2} \qquad (27)$$

Eq.(26) and Eq.(27) show that the components of specific stresses $\Sigma_a, \Sigma_e, \Sigma_i$ and Σ_c linked respectively to warp yarns, weft yarns, interaction between yarns and isotropic part of the coating, are scalars and must be described by scalar constitutive laws. Concerning the deviatoric part of the coating stress, $\underset{\sim}{\overline{\boldsymbol{\Sigma}}_c}$ is a tensor and must be described by a tensorial constitutive law.

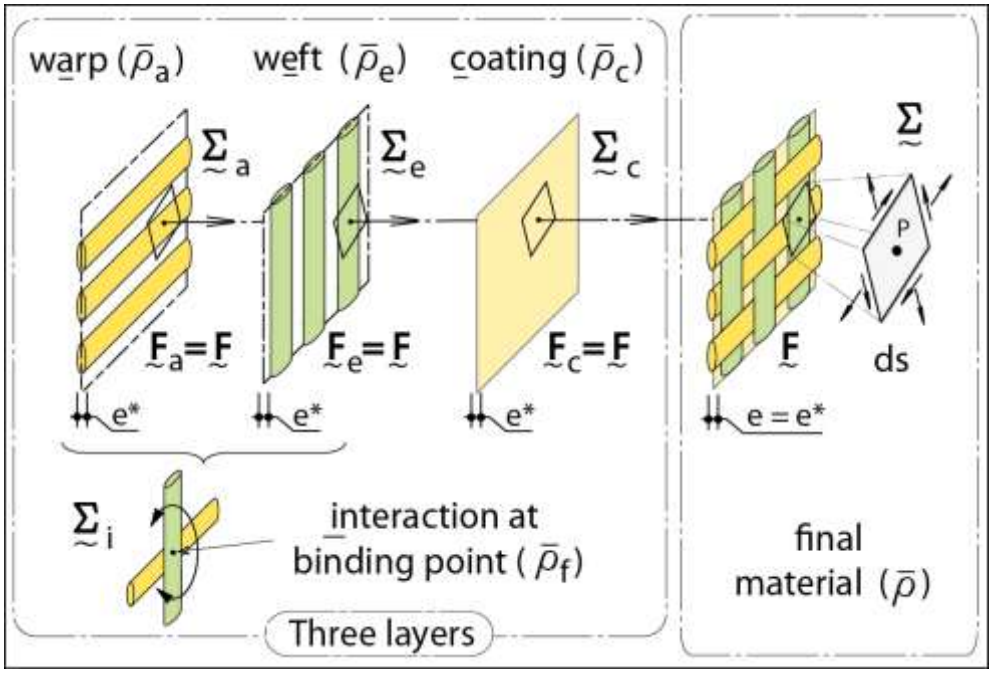

Fig. 3. The material under consideration appears to be the superimposition of two layers of yarns and a coating layer, which have the same deformation ($\mathbf{F} = \mathbf{F_a} = \mathbf{F_e} = \mathbf{F_c}$). Around a material point P, each layer is defined by its specific stress, respectively $\mathbf{\Sigma_a}$, $\mathbf{\Sigma_e}$and $\mathbf{\Sigma_c}$ and its mass per unit surface, respectively $\overline{\rho}_a, \overline{\rho}_e$and $\overline{\rho}_c$. The interaction between yarns, at binding points, is characterized by a specific stress $\mathbf{\Sigma_i}$and by a mass per unit surface $\overline{\rho}_f = \overline{\rho}_a + \overline{\rho}_e$.

Thus, the proposed modelling approach puts forward a scalar modelling for the description of the behaviour of elementary components of material, which correspond to the yarns through Σ_a, Σ_e, to the isotropic part of the coating behaviour through Σ_c and to their interactions through Σ_i. This scalar modelling is developed in section 3. The 2D tensorial modelling about the deviatoric part of the coating behaviour $\overline{\mathbf{\Sigma}}_c$ will be the object of the section 4.

3. One-dimensional constitutive models for yarns and coating

3.1. General formalism

From now on and according to the woven material considered in this paper, the letter "x" will be assigned to "a" when considering the w**a**rp yarns, to "e" when considering the w**e**ft yarns and to "c" when considering the isotropic part of the **c**oating behaviour.

The one-dimensional modelling approach for the mechanical behaviour of the different elementary components of the woven material, adopted in this paper, is inspired by previous works of the authors that put forward the assumption of stress superimposition, corresponding to different physical phenomena that occur when a material undergoes mechanical actions (see for instance, Bles et al. (2009)). In our framework, our approach is of visco-elasto-plastic type built with the superimposition of two stress contributions corresponding to (i) a non-Newtonian visco-elastic behaviour and (ii) an irreversible behaviour of elasto-plastic type. Thus, the total specific stress Σ_x in an elementary component "x" is composed by the sum of a visco-elastic specific stress $\Sigma_{x,v}(\dot{\varepsilon}_x)$, which depends on the strain rate $\dot{\varepsilon}_x$, and of a time-independent stress $\Sigma_{x,h}(\varepsilon_x)$, which depends on the loading history, linked to an irreversible behaviour, such as (Fig. 4):

$$\Sigma_x(\varepsilon_x, \dot{\varepsilon}_x) = \Sigma_{x,v}(\dot{\varepsilon}_x) + \Sigma_{x,h}(\varepsilon_x) \qquad (28)$$

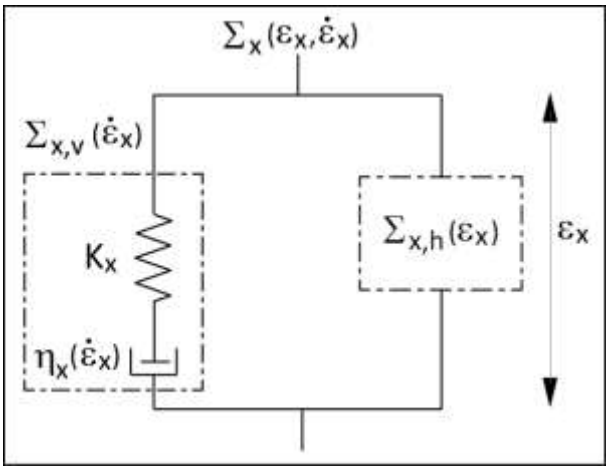

Fig. 4. Model adopted for the description of the mechanical behaviour of any element "x"among yarns and coating. The total specific stress $\Sigma_x(\varepsilon_x, \dot{\varepsilon}_x)$ is composed of a visco-

elastic contribution · (described by a model of Maxwell type) and a time-independent stress linked to an irreversible behaviour.

Let us note that in the case of the yarns, when or e, · can stand for an uni-axial tensile or compression stress. In the case of the coating, when c, · can represent an equi-biaxial isotropic tensile or compression stress.

3.2. Viscoelastic behaviour modelling

The viscoelastic specific stress · is described by a model of Maxwell type, endowed with a variable viscosity · according to the strain rate $\dot{\varepsilon}_x$. This model is defined by a scalar differential equation and this formulation remains the same whatever the considered component" :

— — (29)
$\dot{\varepsilon}_x$

where, denotes the stress rate ; · and are variables defined in Table 2 for each component of the material. In the case of yarns, and are two parameters which express elastic moduli, in the warp direction and the weft direction, respectively. In the case of coating, the parameter denotes a surface bulk modulus. Let us note that for the coating, the rate variables $\dot{\varepsilon}_x$ and are defined from the first invariant of the strain rate tensor in the membrane plane, that is). For yarns, strain rate is defined as the one in the warp direction $\dot{\varepsilon}_a$ and the weft direction $\dot{\varepsilon}_e$, respectively.

Component " x "		$\dot{\varepsilon}$	
Yarns (w**a**rp)		$\dot{\varepsilon}$	
Yarns (w**e**ft)		$\dot{\varepsilon}$	

Coating (Isotropic part)	$2\,K_c$	$I_{\underset{\sim}{D}}$	$I_{\underset{\sim}{D}}/2$

Table 2. Expressions of the variables K_x, $\dot{\varepsilon}_x$ and D_x for the different elementary components of the material.

The viscosity evolution $\eta_x(\dot{\varepsilon}_x)$ is defined by a five parameters Carreau-Yasuda law (see Yasuda. (1979)). This law is described by two regimes: a Newtonian plateau where the viscosity remains constant when the strain rate $\dot{\varepsilon}_x$ tends to zero and a linear regime for intermediate values of $\dot{\varepsilon}_x$, which corresponds to Ostwald and De-Waele power law (see Bird et al. (1977)). If $\dot{\varepsilon}_x$ tends to the infinite, the viscosity tends to zero. The viscosity $\eta_x(\dot{\varepsilon}_x)$ is given by the following equation (Fig. 5):

$$\frac{\eta_x(\dot{\varepsilon}_x)-\eta_{x_\infty}}{\eta_{x_0}-\eta_{x_\infty}} = \{1 + (\lambda_x.|\dot{\varepsilon}_x|)^{a_x}\}^{\frac{n_x-1}{a_x}} \qquad (30)$$

where, η_{x_0} is the constant viscosity of the Newtonian plateau, η_{x_∞} is the viscosity value for infinite strain rate (in our framework, we consider $\eta_{x_\infty} = 0$); λ_x and n_x are parameters that define respectively the threshold and the slope of the Ostwald and De-Waele power law of $\eta_x(\dot{\varepsilon}_x)$ for intermediate values of $\dot{\varepsilon}_x$ and a_x is a transition parameter that acts on the curve shape between constant and linear parts. Fig.5 illustrates the Carreau-Yasuda model, using logarithmic scales and describes the influence of the parameters n_x, λ_x and a_x. Considering the elementary components of the material, i.e. warp yarns, weft yarns and the coating, the modelling proposed here involves 12 parameters: $(\eta_{a_0}, \lambda_a, n_a, a_a)$, $(\eta_{e_0}, \lambda_e, n_e, a_e)$ and $(\eta_{c_0}, \lambda_c, n_c, a_c)$ respectively, through the same scalar law defined by Eq. (30).

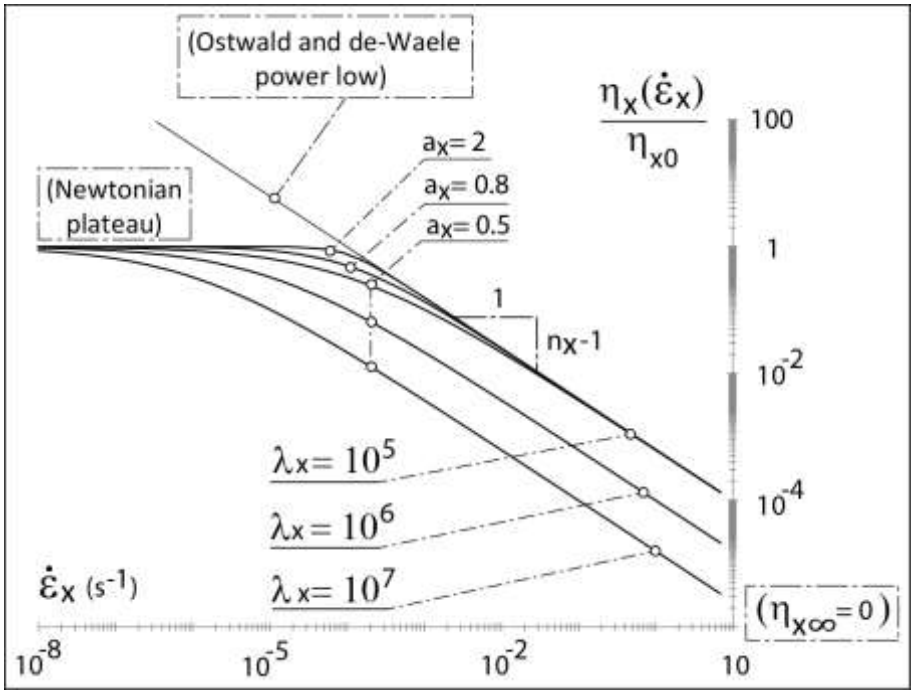

Fig. 5. The viscosity evolution as a function of the strain rate, following the Carreau-Yasuda model defined by Eq. (30) and the influence of the parameters n_x, λ_x and a_x.

3.3. Irreversible time-independent behaviour modelling

3.3.1. General formulation

For each elementary component "x" of the material, the irreversible time-independent specific stress $\Sigma_{x,h}(\varepsilon_x)$ is defined with a behaviour scheme that involves the addition of two non-linear elastic-type laws $\mathcal{L}_{x,1}(\varepsilon_x^R)$, $\mathcal{L}_{x,2}(\Delta\varepsilon_x)$ and the use of a behaviour criterion. The law $\mathcal{L}_{x,1}(\varepsilon_x^R)$ describes the stress state during first load in traction, and only depends on the actual strain $\varepsilon_x^R = \varepsilon_x$, that evolves upon loading. The law $\mathcal{L}_{x,2}(\Delta\varepsilon_x)$ describes a part of the stress state during a cycle (unloading/reloading steps), performed during a traction or compression loading and depends on the variation $\Delta\varepsilon_x$ between a reference strain ε_x^R and the actual strain ε_x such as $\Delta\varepsilon_x = \varepsilon_x - \varepsilon_x^R$. During a cycle, the reference strain ε_x^R corresponds to the memorised strain at inversion point, localised at the end of the first load ; ε_x^R is kept constant

during all the cyclic sequence, its value can only evolve through a return to a sequence of first load. Thus, we define $\Sigma_{x,h}(\varepsilon_x)$ such as:

$$\Sigma_{x,h}(\varepsilon_x) = \mathcal{L}_{x,1}(\varepsilon_x^R) + \mathcal{L}_{x,2}(\Delta\varepsilon_x) \qquad (31)$$

To illustrate the above Eq.(31) and the proposed behaviour scheme, Table 3 gives the structure of $\Sigma_{x,h}(\varepsilon_x)$ for all the possible loading processes. We consider (i) a first load from the initial state in traction and (ii) cycles (unloading /reloading), that can be performed during the loading history. Otherwise, in the case of a simple tensile test on a woven material, in the yarns warp or weft direction, the material undergoes a transverse contraction and the corresponding yarns are in compression. The mechanical laws of yarns and coating should present a well-defined behaviour in compression. Consequently, we also have to consider the loading process of simple compression from the initial state. During the first load, the reference strain corresponds to the actual strain ($\varepsilon_x^R = \varepsilon_x$). Therefore the variation $\Delta\varepsilon_x$ is null ($\Delta\varepsilon_x = 0$) and $\mathcal{L}_{x,2}(\Delta\varepsilon_x) = 0$. Thus, the definition of the total specific stress results from the first law such as: $\Sigma_{x,h}(\varepsilon_x) = \mathcal{L}_{x,1}(\varepsilon_x)$. After an inversion, during a cyclic sequence, the reference strain memorizes the strain at inversion point and takes a constant value ($\varepsilon_x^R = cst$), which corresponds with the constant value of the total specific stress at inversion point $\Sigma_{x,h}(\varepsilon_x^R) = \mathcal{L}_{x,1}(\varepsilon_x^R) = cst$. Thus, during a cyclic sequence, the definition of the total specific stress results from the law $\mathcal{L}_{x,2}(\Delta\varepsilon_x)$, such as: $\Sigma_{x,h}(\varepsilon_x) = cst + \mathcal{L}_{x,2}(\Delta\varepsilon_x)$. Concerning the compression from the initial state, we adopt a reversible elastic behaviour.

Behaviour type	Loading type	$\mathcal{L}_{x,1}(\varepsilon_x^R)$	$\mathcal{L}_{x,2}(\Delta\varepsilon_x)$
Irreversible	First load from initial state in traction	$(\varepsilon_x^R = \varepsilon_x)$; $\mathcal{L}_{x,1}(\varepsilon_x) \neq 0$	$(\Delta\varepsilon_x = 0)$; $\mathcal{L}_{x,2}(0) = 0$

	Cycles (unloading/reloading)	$(\varepsilon_x^R = cst); \mathcal{L}_{x,1}(\varepsilon_x^R) = cst$	$(\Delta\varepsilon_x \neq 0); \mathcal{L}_{x,2}(\Delta\varepsilon_x) \neq 0$
Reversible	Compression from initial state	Elastic behaviour	

Table 3. Structure of $\Sigma_{x,h}(\varepsilon_x)$ during different loading processes.

Fig.6-a illustrates the proposed behaviour scheme, through a rheological pattern, composed of a behaviour criterion and three separate behaviours, used to define the irreversible time-independent specific stress $\Sigma_{x,h}(\varepsilon_x)$. Fig.6-b gives a schematic example of response for $\Sigma_{x,h}(\varepsilon_x)$ as a function of a strain history 0D0ABAC, putting forward the role of the laws $\mathcal{L}_{x,1}$, $\mathcal{L}_{x,2}$ and the behaviour criterion. Let us note that the irreversibility of $\Sigma_{x,h}(\varepsilon_x)$ is generated by the behaviour criterion, despite the reversible character of the laws $\mathcal{L}_{x,1}$ and $\mathcal{L}_{x,2}$. This criterion is expressed in Table 4 and illustrated by Fig.6-b.

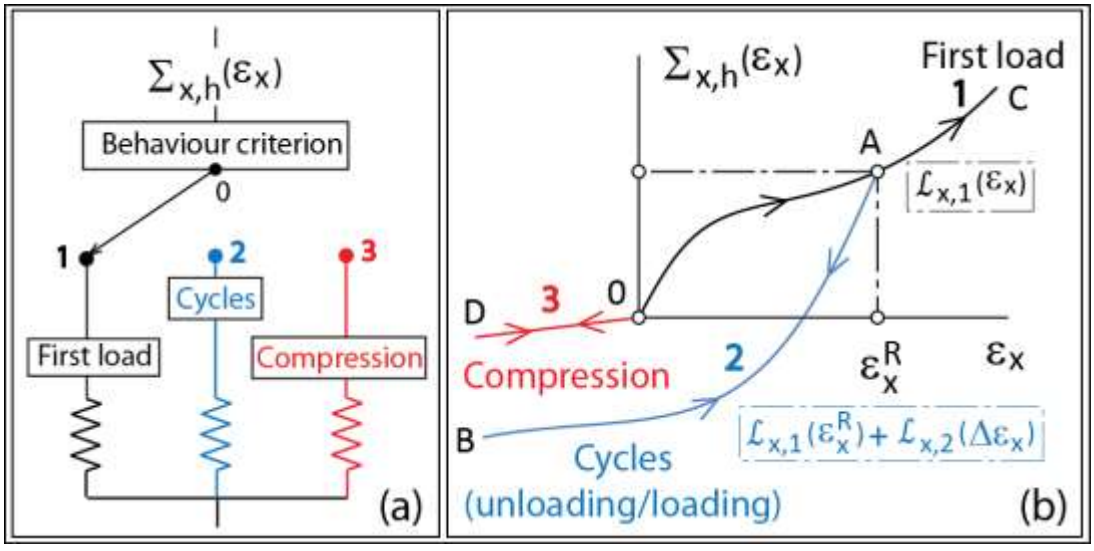

Fig. 6. Rheological pattern with the three behaviours taken into account within the definition of the irreversible time-independent specific stress $\Sigma_{x,h}(\varepsilon_x)$ (a), and a schematic example of response involving the role of the laws $\mathcal{L}_{x,1}$ and $\mathcal{L}_{x,2}$ (b).

Time	ε_x	State	Illustration
t=0	$\varepsilon_x(t) = 0$	Initial state, $\varepsilon_x^R = \varepsilon_x = 0$	Point 0, Fig.6-b
t > 0	$\varepsilon_x(t) < 0$ and $\varepsilon_x^R = 0$	Compression behaviour from initial state	Path 0D0,Fig.6-b
	$\varepsilon_x(t) \geq \varepsilon_x^R(t - dt)$	First load, $\varepsilon_x^R(t) = \varepsilon_x(t)$	Paths 0A and AC, Fig.6-b
	Inversion criterion, $\varepsilon_x(t) < \varepsilon_x^R(t - dt)$	Inversion and cyclic behaviour, $\varepsilon_x^R(t) = \varepsilon_x^R(t - dt)$	Inversion point A and cyclic path ABA, Fig.6-b

Table 4. Behaviour criterion used to define $\Sigma_{x,h}(\varepsilon_x)$. (t: denotes time; dt: denotes an infinitesimal increment of time)

3.3.2. Irreversible time-independent behaviour of the yarns

During the first load from the origin, the irreversible behaviour of yarns is described by a non-linear elastic-type law $\mathcal{L}_{x,1}(\varepsilon_x^R)$ with $\varepsilon_x^R = \varepsilon_x$ that depends on five material parameters, such as:

$$\mathcal{L}_{x,1}(\varepsilon_x^R) = (G_x - L_x).\varepsilon_x^*.\tanh\left(\frac{\varepsilon_x^R}{\varepsilon_x^*}\right) + L_x.\varepsilon_x^R + H_x.(\varepsilon_x^R)^2 + N_x.(\varepsilon_x^R)^3 \qquad (32)$$

where G_x stands for the elastic modulus at the origin and ε_x^* is the strain at the elbow of the hyperbolic tangent function and coincides with the intersection of the modulus at the origin and the threshold to infinity. Concerning the other parameters L_x, H_x and N_x, several cases can occur. If $G_x = L_x$, the first term in the hyperbolic tangent function disappears and then, the non-linear elastic law is a cubic polynomial function, or a quadratic polynomial function if moreover N_x is null. In the particular case where $G_x = L_x$ and $N_x = H_x = 0$, we obtain a linear elastic law whose the modulus is G_x.If $G_x \neq L_x$, the first term in the hyperbolic tangent

function takes part in the law and in that case, if $N_x = H_x = L_x = 0$, this term is the only one that is involved.

The yarns irreversible behaviour during cycles is described by a non-linear elastic law $\mathcal{L}_{x,2}(\Delta\varepsilon_x)$, that is formulated by:

$$\mathcal{L}_{x,2}(\Delta\varepsilon_x) = \frac{\mathcal{L}_{x,1}(\varepsilon_x^R)}{tanh\left(\frac{\varepsilon_x^R}{f_x^*(\varepsilon_x^R)}\right)}.tanh\left(\frac{\Delta\varepsilon_x}{f_x^*(\varepsilon_x^R)}\right) + M_x.\Delta\varepsilon_x \qquad (33)$$

Where $\Delta\varepsilon_x = \varepsilon_x - \varepsilon_x^R$, and ε_x^R is the reference strain memorized at the inversion point; $M_x$is a constant parameter that can be seen as a modulus. Fig.7 illustrates the definitions of the laws $\mathcal{L}_{x,1}$ and $\mathcal{L}_{x,2}$ given by Eq.(32) and Eq.(33) and also, the functioning of the behaviour criterion defined by Table 4. In this illustration, we have chosen compression behaviour from the initial state as a linear elastic behaviour defined by the modulus M_x. According to Eq.(33), the modulus at the inversion point, along the unloading curve is expressed by:

$$\frac{d\mathcal{L}_{x,2}}{d\varepsilon_x}(\Delta\varepsilon_x = 0) = \frac{\mathcal{L}_{x,1}(\varepsilon_x^R)}{tanh\left(\frac{\varepsilon_x^R}{f_x^*(\varepsilon_x^R)}\right)}.\frac{1}{f_x^*(\varepsilon_x^R)} + M_x \qquad (34)$$

The experimental results show that this modulus at inversion evolves as a function of the value of ε_x^R, the memorized strain at inversion (see Bles et al. (2009)). In order to take into account this phenomenon, the function $f_x^*(\varepsilon_x^R)$ is defined by:

$$\frac{1}{f_x^*(\varepsilon_x^R)} = A_x.\frac{\varepsilon_x^R}{\mathcal{L}_{x,1}(\varepsilon_x^R)}.\frac{d\mathcal{L}_{x,1}}{d\varepsilon_x}(\varepsilon_x^R) \qquad (35)$$

where A_x is a non-unit parameter. Eq.(35) determines the evolution of the modulus at inversion point along the unloading curve $\frac{d\mathcal{L}_{x,2}}{d\varepsilon_x}(0)$, as a function of the ratio between the modulus just before the inversion point $\frac{d\mathcal{L}_{x,1}}{d\varepsilon_x}(\varepsilon_x^R)$ and the sequent modulus $\frac{\mathcal{L}_{x,1}(\varepsilon_x^R)}{\varepsilon_x^R}$.

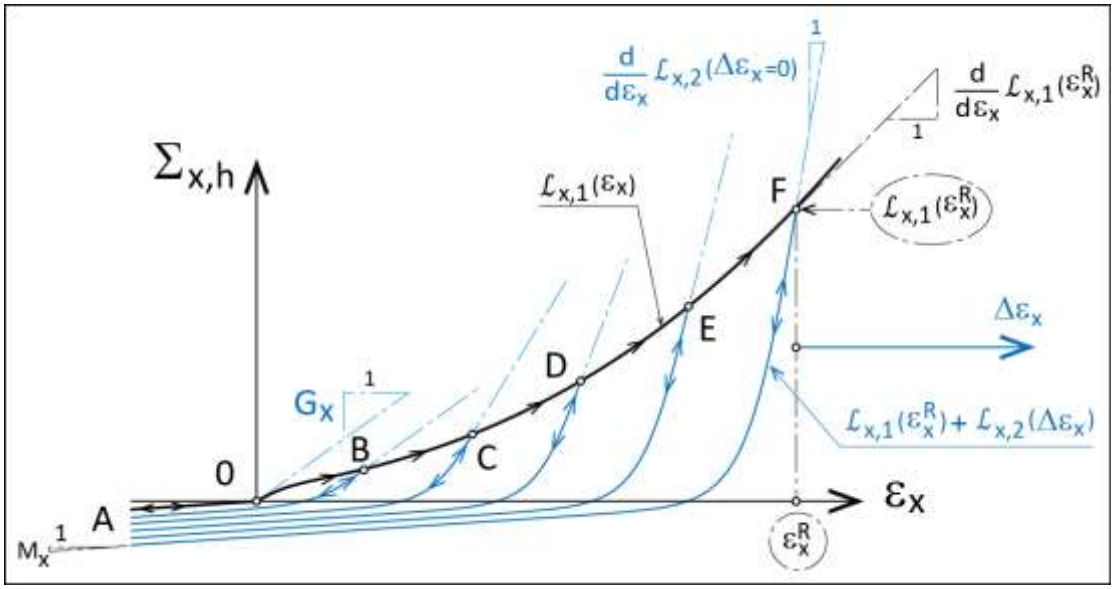

Fig. 7. Illustration of the laws and , defined by Eq.(32) and Eq.(33).

In order to model the yarns behaviour in compression in the vicinity of the origin, we adopted the hypothesis of a linear elastic law. Therefore, the specific stress in the case of yarns in compression can be expressed such as:

and (36)

where is the elastic modulus in compression for the yarns ". In the situation where the yarns are straight (weft yarns) and do not show any crimp, we put forward an hypothesis where the stiffness in compression is the same as in traction in the vicinity of the origin . In the case of the warp yarns, if we take into account the crimp phenomenon, we neglected the stiffness in compression compared to its tensile rigidity). Fig.8 describes schematically the compression modulus and the tensile modulus of both warp and weft yarns.

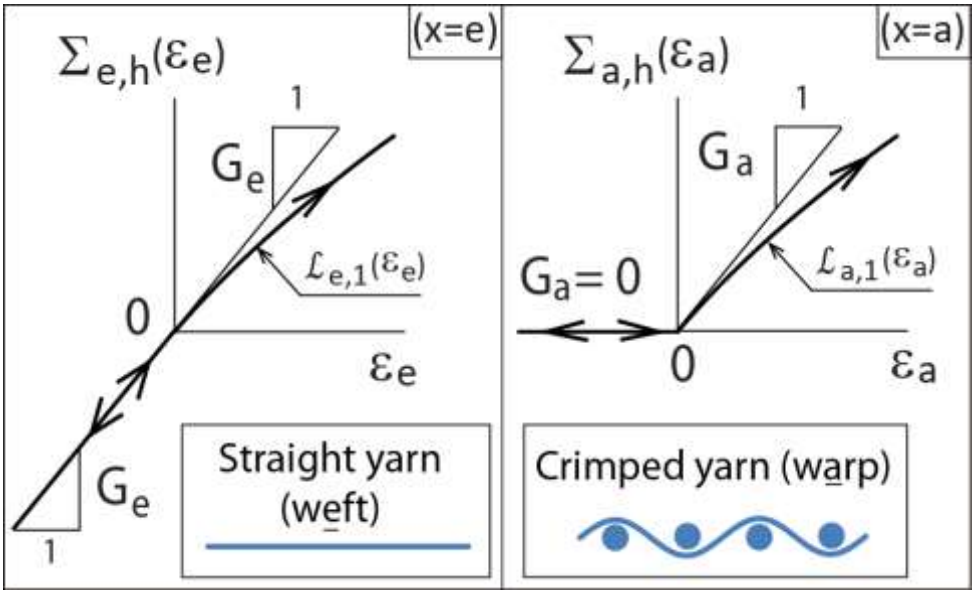

Fig.8. Schematic description of the compression and tensile modulus for weft straight yarns and warp yarns presenting a crimp.

3.3.3. Irreversible time-independent behaviour of the isotropic part of the coating

Here, the index "x" is assigned to the letter "c" and denotes the isotropic part of the coating behaviour. The corresponding strain ε_c indicates the average strain such as:

$$\varepsilon_c = \frac{tr(\underset{\sim}{\boldsymbol{\varepsilon}})}{2} \qquad (37)$$

Where $\underset{\sim}{\boldsymbol{\varepsilon}}$ is the left Hencky tensor. Consequently, Eq.(31) can be written:

$$\Sigma_{c,h}(\varepsilon_c) = \mathcal{L}_{c,1}(\varepsilon_c^R) + \mathcal{L}_{c,2}(\Delta\varepsilon_c) \qquad (38)$$

During the first load from the origin, the isotropic part of the coating specific stress $\Sigma_{c,h}(\varepsilon_c)$ is described by the non-linear elastic-type law $\mathcal{L}_{c,1}(\varepsilon_c^R)$ with $\varepsilon_c^R = \varepsilon_c$, such as:

$$\mathcal{L}_{c,1}(\varepsilon_c^R) = 2.(K_1 - K_2).f(\varepsilon_c^R).\varepsilon_c^R + 2.K_2.\varepsilon_c \qquad (39)$$

Where K_1 is the surface bulk modulus at the origin; K_2 is the surface bulk modulus describing the slope of $\mathcal{L}_{c,1}(\varepsilon_c^R)$ when ε_c^R tends to high values; $f(x)$ is a function used to make evolve the modulus, such as:

$$f(x) = \frac{tanh(x/x^*)}{x/x^*} \qquad (40)$$

where x^* is a constant parameter corresponding to the variable x. Fig.9 shows the graph of the function $f(x)$ as a function of x/x^*. In this case of isotropic part of the coating behaviour x^* is assigned to a parameter ε_c^*, which represents the strain at the elbow of the hyperbolic tangent function.

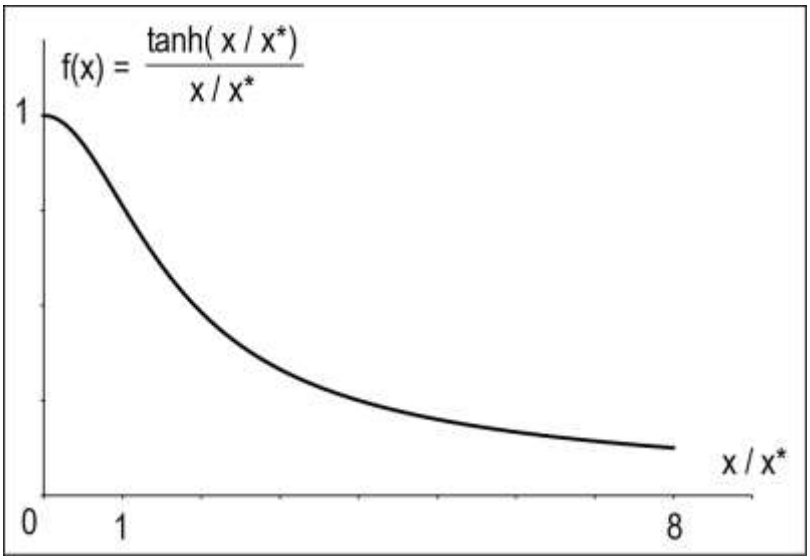

Fig.9. Graph of the function $f(x)$ versus x/x^*.

Fig.10. illustrates the evolution of the non-linear elastic-type law $\mathcal{L}_{c,1}(\varepsilon_c^R)$ during the first load from the origin ($\varepsilon_c^R = \varepsilon_c$), describing the irreversible time-independent specific stress $\Sigma_{c,h}(\varepsilon_c)$ corresponding to the isotropic part of the coating behaviour. During cycles, the isotropic part of the coating irreversible behaviour is described by the linear elastic law $\mathcal{L}_{c,2}(\Delta\varepsilon_c)$, that is formulated by :

$$\mathcal{L}_{c,2}(\Delta\varepsilon_c) = 2.(K_3 - K_2).\Delta\varepsilon_c \qquad (41)$$

Where $\Delta\varepsilon_c = \varepsilon_c - \varepsilon_c^R$, and ε_c^R denotes the average strain memorized at inversion point and takes a constant value during cycles. Thus, the final expression of $\Sigma_{c,h}(\varepsilon_c)$ can be written as follows:

$$\Sigma_{c,h}(\varepsilon_c) = 2.(K_1 - K_2).f(\varepsilon_c^R).\varepsilon_c^R + 2.(K_3 - K_2).\Delta\varepsilon_c + 2.K_2.\varepsilon_c \qquad (42)$$

In compression, we adopted the hypothesis of a linear elastic law. The specific stress can be expressed such as:

$$\Sigma_{c,h}(\varepsilon_c) = 2.K_3.\varepsilon_c \quad \text{and} \quad \varepsilon_c(t) < 0 \qquad (43)$$

Fig.10 illustrates the evolution of the irreversible time-independent specific stress $\Sigma_{c,h}(\varepsilon_c)$, during a loading history 0A0BCBD.

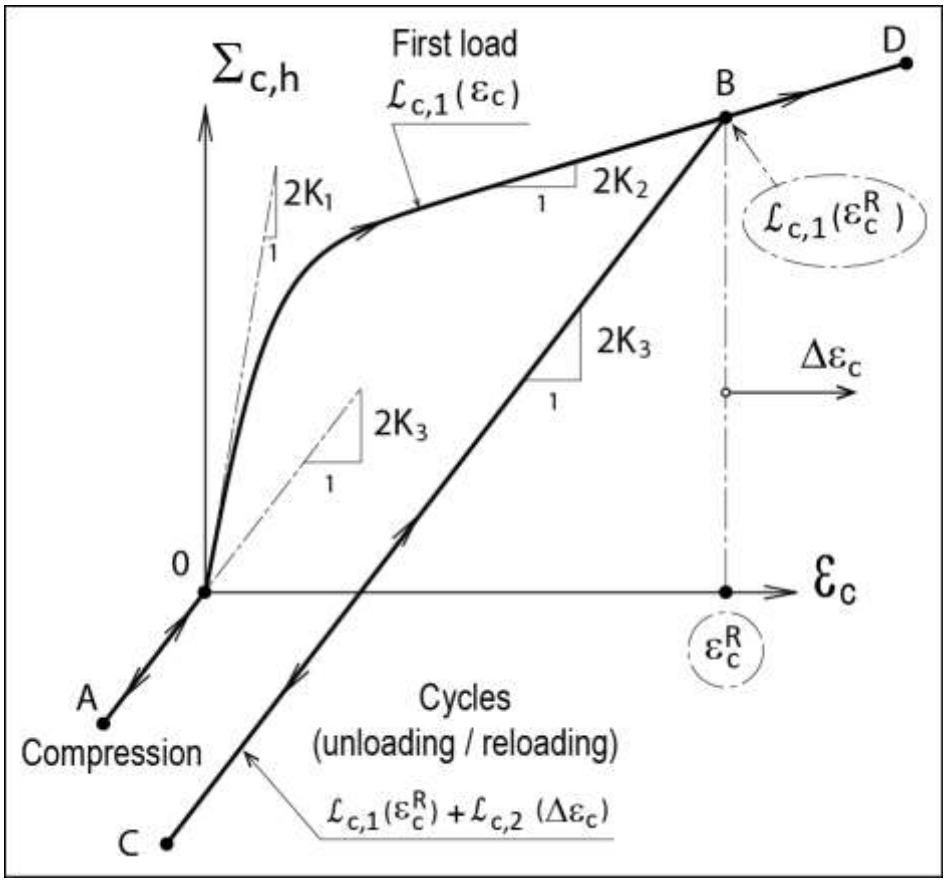

Fig.10. Typical evolution of $\Sigma_{c,h}(\varepsilon_c)$.

3.4. Modelling of the yarns interaction

The works of Boisse et al (2006) showed that the interaction behaviour between the yarns is a non-linear behaviour. This behaviour can be represented by two linear laws between the interaction specific stress Σ_i and the distortion angle γ. Those both laws are distinguished by a low stiffness for distortion angles below the shear-locking angle and by a much higher stiffness for angles of higher values. For the family of materials for which we are interesting in this work, the value of distortion angle remains low even for loadings close to fracture. For this, we are positioned below the value of the shear-locking angle and we adopt a linear law to describe the **i**nteraction behaviour between two yarns at a binding point, such that:

$$\Sigma_i(\varepsilon_\gamma) = K_\gamma . \varepsilon_\gamma \qquad (44)$$

Where K_γ is an elastic modulus and ε_γ the distortion strain. The choice of ε_γ for the model definition was motivated by the definition itself of this strain, that is linked to the value of angle between the yarns (cf. Eq.(15)). We will see in section 5.1, concerning the identification of the model that the coupling between the different components of the material leads to complex manifestations of the interaction behaviour between the yarns, despite the simplicity of the law (44).

4. Tensorial constitutive law of the deviatoric part of coating behaviour

4.1 General formulation

In this part, we now focus on the 2D tensorial modelling of the deviatoric part of the coating behaviour under cyclic biaxial loadings. Here, we put forward a 2D visco-elasto-plastic model. The deviatoric specific stress tensor in the coating $\underset{\sim}{\boldsymbol{\Sigma}}_{\boldsymbol{c}}$ results from the

superimposition of (i) a non-Newtonian visco-elastic behaviour $\underset{\sim}{\overline{\boldsymbol{\Sigma}}}_{\boldsymbol{c,v}}$ and (ii) an irreversible behaviour of elasto-plastic type $\underset{\sim}{\overline{\boldsymbol{\Sigma}}}_{\boldsymbol{c,h}}$, such as:

$$\underset{\sim}{\overline{\boldsymbol{\Sigma}}}_{\boldsymbol{c}} = \underset{\sim}{\overline{\boldsymbol{\Sigma}}}_{\boldsymbol{c,v}} + \underset{\sim}{\overline{\boldsymbol{\Sigma}}}_{\boldsymbol{c,h}} \qquad (45)$$

The visco-elastic contribution of the specific stress $\underset{\sim}{\overline{\boldsymbol{\Sigma}}}_{\boldsymbol{c,v}}$ will be defined in the subsection 4.2 and the time-independent irreversible contribution $\underset{\sim}{\overline{\boldsymbol{\Sigma}}}_{\boldsymbol{c,h}}$ will be described in the subsection 4.3.

4.2 Viscoelastic behaviour modelling

The deviatoric visco-elastic specific stress of the coating $\underset{\sim}{\overline{\boldsymbol{\Sigma}}}_{\boldsymbol{c,v}}$ is also defined according to a model of Maxwell type, through a tensorial differential equation such as:

$$\frac{\overset{\circ}{\underset{\sim}{\overline{\boldsymbol{\Sigma}}}}_{\boldsymbol{c,v}}}{2\mu_v} + \frac{\underset{\sim}{\overline{\boldsymbol{\Sigma}}}_{\boldsymbol{c,v}}}{\eta_d\left(Q_{\underset{\sim}{\boldsymbol{D}}}\right)} = \underset{\sim}{\overline{\boldsymbol{D}}} \qquad (46)$$

where $\overset{\circ}{\underset{\sim}{\overline{\boldsymbol{\Sigma}}}}_{\boldsymbol{c,v}}$ denotes the objective stress rate of Green-Naghdi; μ_v is a constant shear modulus; $\underset{\sim}{\overline{\boldsymbol{D}}}$ is the deviatoric part of the strain rate tensor $\underset{\sim}{\boldsymbol{D}}$ and $\eta(Q_{\underset{\sim}{\boldsymbol{D}}})$ is a variable viscosity according to $Q_{\underset{\sim}{\boldsymbol{D}}}$ the radius in the deviatoric plane of the strain rate tensor $\underset{\sim}{\boldsymbol{D}}$ (cf. Appendix A). The viscosity $\eta_d(Q_{\underset{\sim}{\boldsymbol{D}}})$ is described by Eq.(30) of the four parameters $(\eta_{d_0}, \lambda_d, a_d, n_d)$ Carreau-Yasuda law $(\eta_{d_\infty} = 0)$, where the index x is assigned to the letter d and denotes the **d**eviatoric part of the coating behaviour and the corresponding strain rate $\dot{\varepsilon}_x$ is replaced by $Q_{\underset{\sim}{\boldsymbol{D}}}$.

Thus, the viscous behaviour of the coating is described by Eq.(29) and Eq.(46) depending, respectively, on the variable viscosity $\eta_c\left(I_{\underset{\sim}{\boldsymbol{D}}}\right)$ for the isotropic part and the variable viscosity $\eta_d\left(Q_{\underset{\sim}{\boldsymbol{D}}}\right)$ for the deviatoric part. We consider that those both viscosities follow the same

evolution, respectively, as a function of $I_{\underset{\sim}{D}}$ and as a function of $Q_{\underset{\sim}{D}}$, so that the four parameters of the Carreau-Yasuda law are identical ($\eta_{d_0} = \eta_{c_0}, \lambda_d = \lambda_c, a_d = a_c, n_d = n_c$).

4.3 Irreversible time-independent behaviour modelling

Let us consider the representation of the deviator of a 2D symmetric tensor in the deviatoric plane, introduced by Appendix A and Eq.(A.16). This representation enables us to assign to the deviator $\overline{\underset{\sim}{\boldsymbol{\Sigma}}}_{\boldsymbol{c,h}}$, a vector $\vec{\underline{s}}$, and to assign to the deviator $\overline{\underset{\sim}{\boldsymbol{\varepsilon}}}$, a vector $\vec{\underline{e}}$ such as:

$$\vec{\underline{s}} = Q_{\underset{\sim}{\boldsymbol{\Sigma}}_{\boldsymbol{c,h}}} . \vec{u}_{\underset{\sim}{\boldsymbol{\Sigma}}_{\boldsymbol{c,h}}} \qquad \text{and} \qquad \vec{\underline{e}} = Q_{\underset{\sim}{\boldsymbol{\varepsilon}}} . \vec{u}_{\underset{\sim}{\boldsymbol{\varepsilon}}} \qquad (47)$$

Where $Q_{\underset{\sim}{\boldsymbol{\Sigma}}_{\boldsymbol{c,h}}}$ and $Q_{\underset{\sim}{\boldsymbol{\varepsilon}}}$ are the radius in the deviatoric plane of stress and strain respectively; $\vec{u}_{\underset{\sim}{\boldsymbol{\Sigma}}_{\boldsymbol{c,h}}}$ and $\vec{u}_{\underset{\sim}{\boldsymbol{\varepsilon}}}$ are the orientation vectors in the deviatoric plane of stress and strain. The irreversible behaviour of elasto-plastic type corresponding to the stress contribution $\overline{\underset{\sim}{\boldsymbol{\Sigma}}}_{\mathbf{c,h}}$ can be described by a radial type law, by adopting a similar approach to the one proposed in section 3.3.3 (Eq.(38)) for the isotropic part, such as:

$$Q_{\underset{\sim}{\boldsymbol{\Sigma}}_{\boldsymbol{c,h}}} = \mathcal{L}_{\overline{c},1}\left(Q^R_{\underset{\sim}{\varepsilon}}\right) + \mathcal{L}_{\overline{c},2}\left(\Delta Q_{\underset{\sim}{\varepsilon}}\right) \qquad (48)$$

$$\text{and} \qquad \vec{u}_{\underset{\sim}{\boldsymbol{\Sigma}}_{\boldsymbol{c,h}}} = \vec{u}_{\underset{\sim}{\boldsymbol{\varepsilon}}} \qquad (49)$$

Where $\mathcal{L}_{\overline{c},1}$ and $\mathcal{L}_{\overline{c},2}$ are two scalar laws to be defined and $\Delta Q_{\underset{\sim}{\varepsilon}} = Q_{\underset{\sim}{\boldsymbol{\varepsilon}}} - Q^R_{\underset{\sim}{\boldsymbol{\varepsilon}}}$; $Q^R_{\underset{\sim}{\boldsymbol{\varepsilon}}}$ is the reference radius such as $Q^R_{\underset{\sim}{\boldsymbol{\varepsilon}}} = Q_{\underset{\sim}{\boldsymbol{\varepsilon}}}$ for the first load. For an unloading-reloading cycle, $Q^R_{\underset{\sim}{\boldsymbol{\varepsilon}}}$ memorizes the radius in the deviatoric plane of strain at inversion state. Thus, the deviator $\overline{\underset{\sim}{\boldsymbol{\Sigma}}}_{\boldsymbol{c,h}}$, is defined by the law (Eq.(48)) which defines its intensity and the law (Eq.(49)) which characterizes its direction. Unfortunately, the law of Eq.(49) presents a singularity for

strain paths going by the origin of the deviatoric plane. Indeed, according to Eq.(A1-17), the orientation vector $\vec{u}_\varepsilon$ of the representative point in the strain deviatoric plane is written :

$$\vec{u} \quad — \vec{J} + — \vec{K} \qquad (50)$$

for 0, the orientation vector $\vec{u}_\varepsilon$ is not defined. This is illustrated by Fig.11. Indeed, during the first load 0A in the strain deviatoric plane (dotted line on Fig.11), and Eq.(48) and Eq.(49) enable us to define the path in the stress space. At inversion (point A), , where stands for the radius at inversion in A. Going to zero in the strain deviatoric plane, Eq.(49) cannot define the stress orientation vector anymore, which presents a singularity in the definition of the law. Let us note that, still Eq.(49) enables us to define the stress orientation vector in and in 0^+, that leads to a discontinuity in the model response for stress from the point to the point on Fig.11.

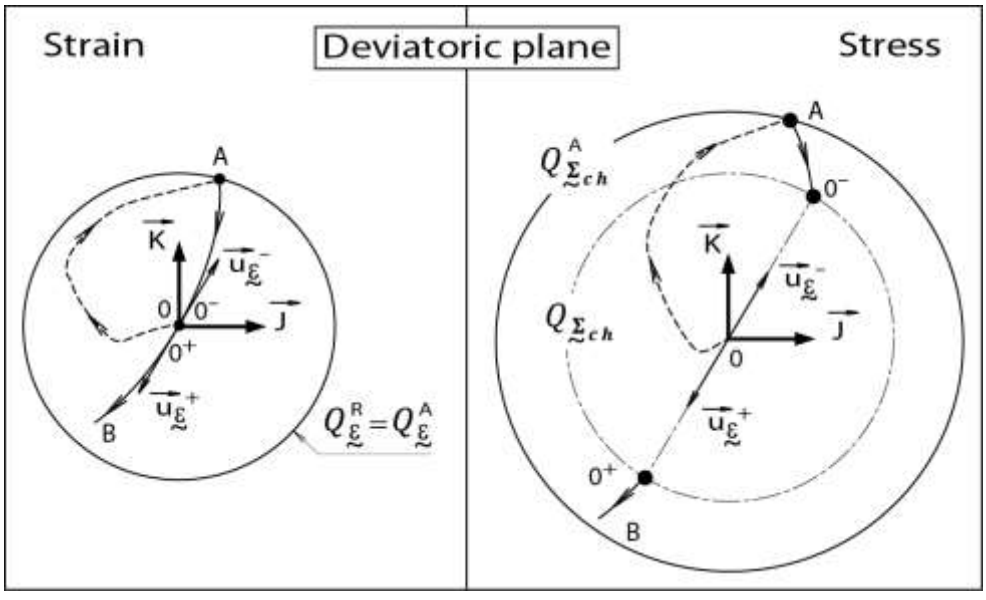

Fig. 11. Singularity and discontinuity of the stress, when the radius of strain state is null.

In order to avoid this singularity, we adopted an octa-directional radial law. This law enables to define the stress direction vector in the deviatoric plane thanks to fixed and previously

defined preferred directions. The octa-directional law puts forward height preferred directions, represented by height unit vectors $\vec{q}_1$ to $\vec{q}_8$(see Fig. 12-a). Those unit vectors are expressed in the deviatoric plane as a function of the vectors $\vec{J}$ and $\vec{K}$ and their modulus $J = \sqrt{2}$ and $K = \sqrt{2}$ (see appendix A), such as :

$$\begin{gathered}\vec{q}_1 = \frac{\vec{J}}{J};\ \vec{q}_2 = \frac{\vec{J}+\vec{K}}{\|\vec{J}+\vec{K}\|}\ ;\ \vec{q}_3 = \frac{\vec{K}}{K}\ ;\ \vec{q}_4 = \frac{-\vec{J}+\vec{K}}{\|\vec{J}+\vec{K}\|} \\ \vec{q}_5 = -\vec{q}_1\ ;\ \ \vec{q}_6 = -\vec{q}_2\ \ ;\ \ \vec{q}_7 = -\vec{q}_3\ ;\ \vec{q}_8 = -\vec{q}_4\end{gathered} \tag{51}$$

Those vectors $\vec{q}_i$ stand for deviatoric tensors $\overline{\boldsymbol{Q}}_{\boldsymbol{i}}$ expressed in one point *P* of the coating in an orthonormal basis $(M, \overrightarrow{e_1}, \overrightarrow{e_2})$ of the tangent plane, such as :

$$\begin{gathered}\overline{\boldsymbol{Q}}_{\boldsymbol{1}} = \frac{1}{\sqrt{2}}.\begin{bmatrix}1 & 0\\ 0 & -1\end{bmatrix};\ \overline{\boldsymbol{Q}}_{\boldsymbol{2}} = \frac{1}{\sqrt{2}}.\begin{bmatrix}1 & 1\\ 1 & -1\end{bmatrix} \\ \overline{\boldsymbol{Q}}_{\boldsymbol{3}} = \frac{1}{\sqrt{2}}.\begin{bmatrix}0 & 1\\ 1 & 0\end{bmatrix}\ ;\ \overline{\boldsymbol{Q}}_{\boldsymbol{4}} = \frac{1}{\sqrt{2}}.\begin{bmatrix}-1 & 1\\ 1 & 1\end{bmatrix} \\ \overline{\boldsymbol{Q}}_{\boldsymbol{5}} = -\overline{\boldsymbol{Q}}_{\boldsymbol{1}}\ ;\ \overline{\boldsymbol{Q}}_{\boldsymbol{6}} = -\overline{\boldsymbol{Q}}_{\boldsymbol{2}}\ ;\ \overline{\boldsymbol{Q}}_{\boldsymbol{7}} = -\overline{\boldsymbol{Q}}_{\boldsymbol{3}}\ ;\ \overline{\boldsymbol{Q}}_{\boldsymbol{8}} = -\overline{\boldsymbol{Q}}_{\boldsymbol{4}}\end{gathered} \tag{52}$$

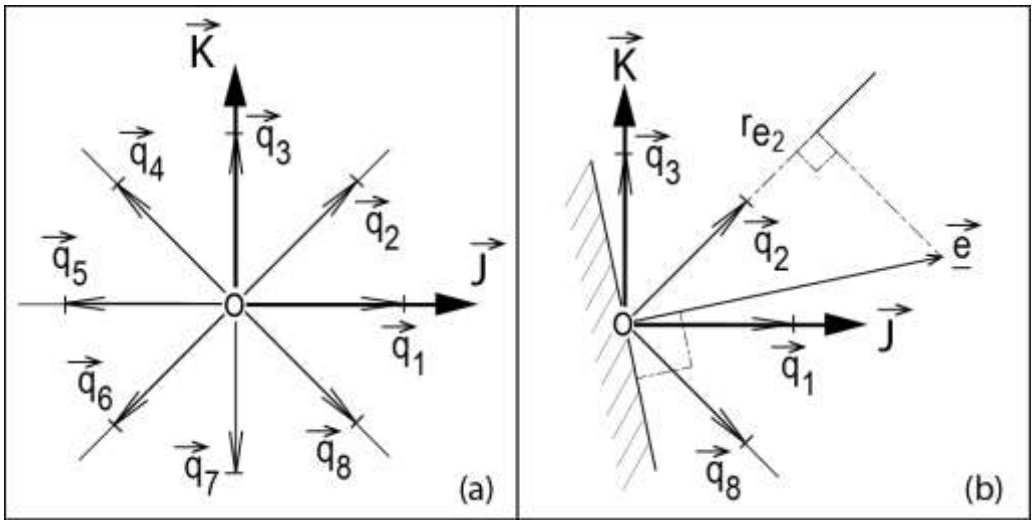

Fig. 12. (a) Representation of the height preferred directions on unit vectors $\overrightarrow{q_1}$ to $\overrightarrow{q_8}$ in the deviatoric plane $(O, \vec{J}, \vec{K})$; (b) Example of projection of a vector $\underline{\vec{e}}$ on the direction $\vec{q}_2$ and definition of the directions that enable the stress calculation according to the orientation of the vector $\underline{\vec{e}}$.

A given strain deviator $\underset{\sim}{\bar{\boldsymbol{\varepsilon}}}$, represented by a vector $\underline{\vec{e}}$ in the strain deviatoric plane, is projected on the height directions $\vec{q}_i$ such as:

$$r_{e_i} = \underline{\vec{e}}.\vec{q}_i \quad \text{or} \quad r_{e_i} = Tr\left(\underset{\sim}{\bar{\boldsymbol{\varepsilon}}}.\overline{\boldsymbol{Q_i}}\right) \quad , \quad (\text{i} = 1 \text{ to } 8) \qquad (53)$$

This enables to determine eight projected strain radius r_{e_i} on the directions $\vec{q}_i$ (for example, r_{e_2} on the direction $\vec{q}_2$ on Fig. 12-b). Those quantities enable the calculation of eight stress radius r_{s_i} thanks to a scalar law (similarly to Eq.(48)), such as:

$$r_{s_i} = \mathcal{L}_{\overline{c},1}\left(r_{e_i}^R\right) + \mathcal{L}_{\overline{c},2}\left(\Delta r_{e_i}\right) \quad , \quad (\text{i} = 1 \text{ to } 8) \qquad (54)$$

Then, the radius r_{s_i} enables the calculation of the stress vector $\underline{\vec{s}}$, such as:

$$\underline{\vec{s}} = \sum_{i=1}^{8} r_{s_i}.\vec{q}_i \qquad (55)$$

Where $\Delta r_{e_i} = r_{e_i} - {r_{e_i}}^R$, and ${r_{e_i}}^R$ is the reference strain radius, along the direction $\vec{q}_i$, such as ${r_{e_i}}^R = r_{e_i}$ during the first load and ${r_{e_i}}^R$ memorizes the strain radius along the direction $\vec{q}_i$ at inversion, during an unloading-reloading cycle. The scalar radial laws $\mathcal{L}_{\overline{c},1}\left(r_{e_i}^R\right)$ and $\mathcal{L}_{\overline{c},2}\left(\Delta r_{e_i}\right)$ of Eq.(54), can be expressed such as :

$$\mathcal{L}_{\overline{c},1}\left({r_{e_i}}^R\right) = \mu_1.f\left({r_{e_i}}^R\right).{r_{e_i}}^R \quad \text{and} \quad \mathcal{L}_{\overline{c},2}(\Delta r_e) = \mu_3.\Delta r_{e_i} \qquad (56)$$

where $f(x)$ is the function of "modulus evolution" previously introduced in Eq.(40) and illustrated on Fig.9. The parameter x^* of $f(x)$ is assigned to a parameter Q_ε^*. Fig.13-a illustrates the model behaviour in projection along a preferred direction $\vec{q}_i$.

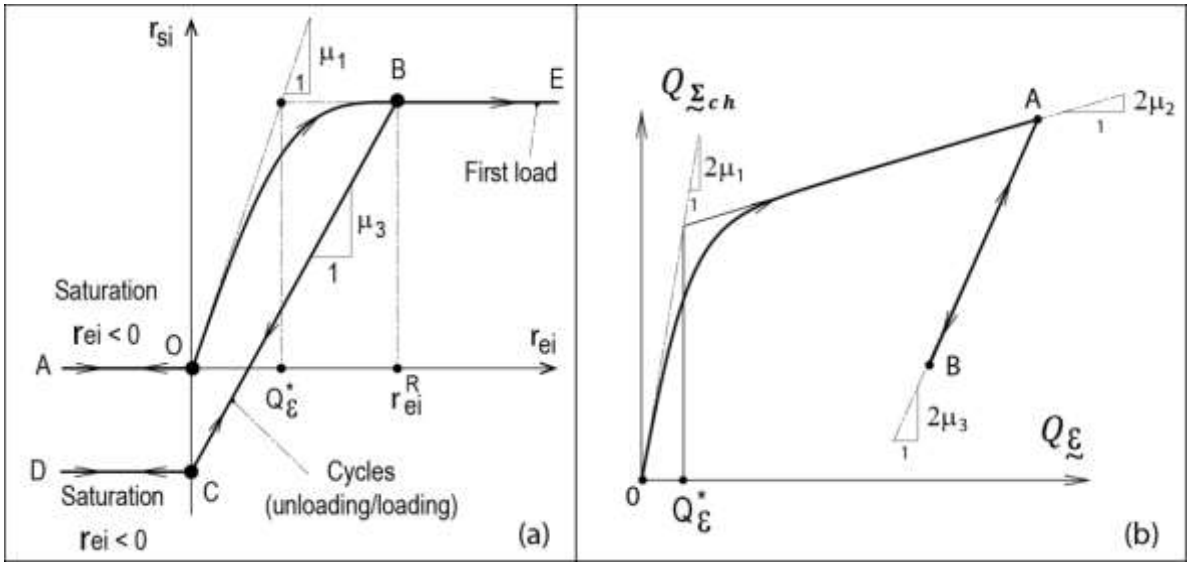

Fig. 13. Illustration of the model behaviour: (a) in projection along a preferred direction $\vec{q}_i$, (b) in a diagram $Q_{\underset{\sim}{\Sigma}_{c,h}} - Q_{\underset{\sim}{\varepsilon}}$.

An inversion and return on the first loading criterion is applied in order to define the ${r_{e_i}}^R$ values. This criterion is described in Table 5. This table shows that if $r_{e_i} < 0$, the projection r_{s_i} is the one obtained for $r_{e_i} = 0$. Consequently, $\Delta r_{e_i} = 0 - {r_{e_i}}^R = -{r_{e_i}}^R$. This behaviour that corresponds with a saturation of the stress in compression is illustrated on Fig.13-a. Starting from the initial state of the material, the consequence of the choice of saturation behaviour is to eliminate the contributions from the vectors $\vec{q}_i$ that present the projections $r_{e_i} < 0$ of the stress calculation as they lead to quantities r_{s_i} that are null. In that case, only the contributions of directions $\vec{q}_i$ that present projection $r_{e_i} \geq 0$ contribute to the stress calculation. This aspect is illustrated by Fig.12-b.

Time	Projections $r_{e_i}(t)$, (i = 1 to 8)	State of the model and ${r_{e_i}}^R(t)$, (i = 1 to 8)	Illustration
$t = 0$	$r_{e_i}(t) = 0$	Initial state ${r_{e_i}}^R = r_{e_i} = r_{s_i} = 0$	Point 0 in Fig. 13

$t > 0$	$r_{e_i}(t) < 0$	Saturation behaviour at $r_{e_i}(t) < 0$ $r_{e_i}{}^R(t) = r_{e_i}{}^R(t - dt)$ and $r_{s_i} = \mathcal{L}_{\bar{c},1}(r_{e_i}^R) + \mathcal{L}_{\bar{c},2}(-r_{e_i}^R) = cst$	Paths OAO and CDC in Fig. 13-a
	$r_{e_i}(t) \geq r_{e_i}{}^R(t - dt)$	Behaviour during the first loading $r_{e_i}{}^R(t) = r_{e_i}(t)$ and $r_{s_i} = \mathcal{L}_1(r_{e_i}{}^R)$	Paths OB and BE in Fig. 13-a
	Inversion criterion $r_{e_i}(t) < r_{e_i}{}^R(t - dt)$	Cyclic behaviour $r_{e_i}{}^R(t) = r_{e_i}{}^R(t - dt)$ and $\Delta r_{e_i} = r_{e_i}(t) - r_{e_i}{}^R(t)$ $r_{s_i} = \mathcal{L}_{\bar{c},1}(r_{e_i}^R) + \mathcal{L}_{\bar{c},2}(\Delta r_{e_i})$	Path BCDCB in Fig. 13-a

Table 5. Inversion criterion and definition of $r_{e_i}{}^R$ and r_{s_i}.

To complete the definition of the radial octa-directional law, we introduce a shear modulus μ_2 describing the slope when $Q_{\underset{\sim}{\boldsymbol{\varepsilon}}}$ tends to high values (see Fig.13-b). Then, in order to describe the behaviour of the irreversible stress $\underset{\sim}{\overline{\boldsymbol{\Sigma}}}_{\boldsymbol{c,h}}$, the model can be summarized by:

$$\underset{\sim}{\overline{\boldsymbol{\Sigma}}}_{\boldsymbol{c,h}} = \sum_{i=1}^{8} r_{s_i} . \overline{\boldsymbol{Q}_{\boldsymbol{i}}} + 2\mu_2 \underset{\sim}{\bar{\boldsymbol{\varepsilon}}} \qquad (57)$$

with

$$\begin{cases} r_{s_i} = (\mu_1 - \mu_2).f(r_{e_i}{}^R).r_{e_i}{}^R + (\mu_3 - \mu_2).\Delta r_{e_i} \\ \Delta r_{e_i} = r_{e_i} - r_{e_i}{}^R \\ r_{e_i} = Tr(\overline{\boldsymbol{\varepsilon}}.\overline{\boldsymbol{Q_i}}) \end{cases} \qquad (58)$$

Eq. (42) and Eq. (58) show that the time-independent irreversible behaviour of the coating presents an isotropic part and a deviatoric part that are decoupled. Indeed, thanks to

function $f(x)$, the elastic moduli evolves, respectively, as a function of $tr(\underset{\sim}{\boldsymbol{\varepsilon}})/2$ for the isotropic part (Eq. (37)) and as a function of the projections r_{e_i} in the deviatoric plane (Eq.(58)) for the deviatoric part. For the coating, we adopt a Poisson ratio ν which enables to convert the elastic moduli couples (K_i, μ_i) $(i = 1,2,3)$ to couples (E_i, ν) such as:

$$K_i = \frac{E_i}{2(1-\nu)} \text{ and } \mu_i = \frac{E_i}{2(1+\nu)} \quad (i = 1,2,3) \qquad (59)$$

where E_i $(i = 1,2,3)$ stand for the three tensile elastic moduli corresponding with the three behaviour zones described by Fig. 10 or Fig. 13-b. Let us note that the expression of the three surface bulk moduli K_i, given by Eq. (59) shows that the surface incompressibility is obtained for a Poisson ratio $\nu = 1$. This is due to the fact that Eq. (59) is obtained by the Hooke isotropic law applied with the membrane hypothesis.

In order to illustrate the complete 2D cyclic behaviour of the coating, which is a visco-elasto-plastic, we consider a biaxial strain loading OABCD, in the $(\varepsilon_{11}, \varepsilon_{22})$ diagram (see Fig.14-a). This loading is considered without any relaxation steps. In that case, the response of the law is represented by the mixed dash line, in the stress diagram $(\Sigma_{11}, \Sigma_{22})$ (see Fig.14-b), in the stress-strain isotropic contributions diagram $(\Sigma_c, \varepsilon_c)$ (see Fig.14-c) and in the stress-strain deviatoric contributions diagram $(q_\Sigma, q_\varepsilon)$ (see Fig.14-d). In a second simulation, we consider a first loading OA, followed by a bi-axial relaxation sequence located at the point A, then we consider three other bi-axial relaxation sequences in B, C and D. During those relaxation sequences, both deformation components ε_{11} and ε_{22} are maintained constant. The positions of these relaxations are assigned to circles on Fig.14. The corresponding response of the model is plotted with a continuous line on Fig.14-b, Fig.14-c and Fig.14-d. On those figures, the beginning of the relaxation sequence is located in A, B, C and D and the end is located in R_1, R_2, R_3 and R_4. We note that on the loading paths AB, BC, CD and DE, one of the strain

components ε_{11} or ε_{22} is maintained constant whilst the other one evolves, which could correspond to a kind of partial relaxation that implies a quite complex response.

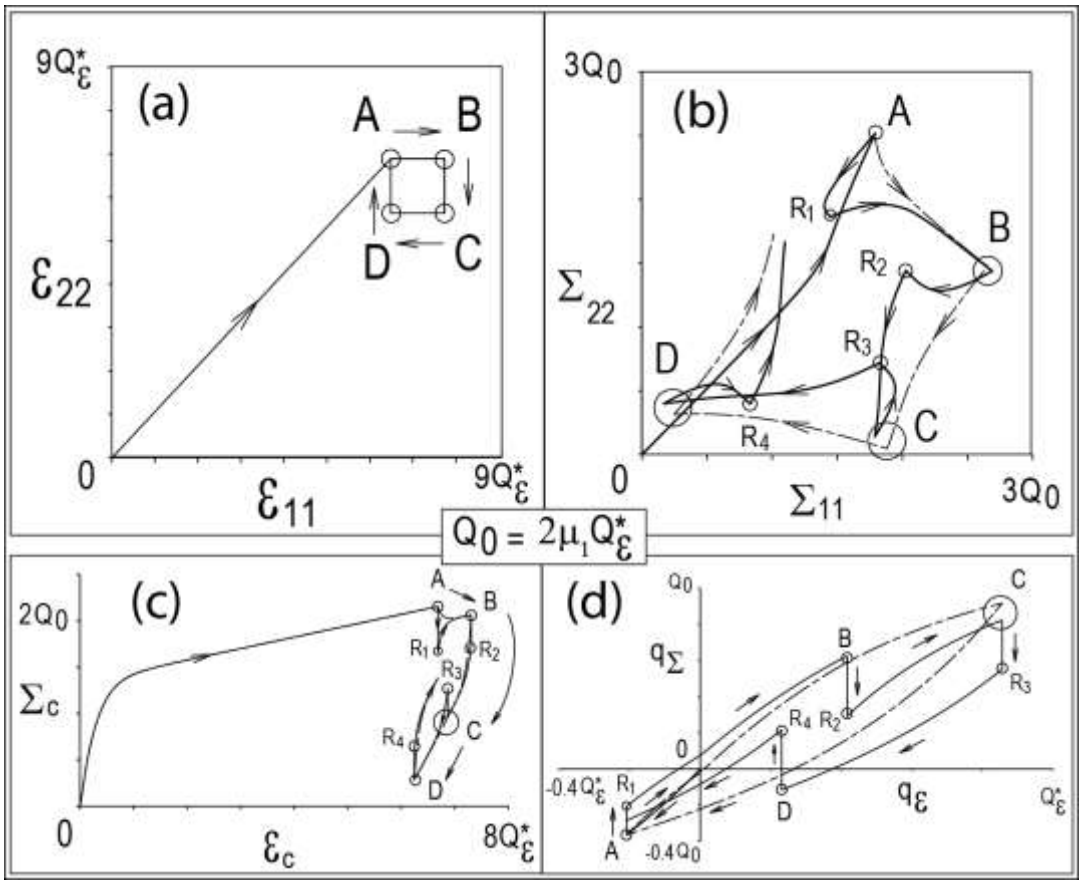

Fig. 14. Complex biaxial strain loading OABCD simulation of the coating behaviour: (a) strain loading in the $(\varepsilon_{11}, \varepsilon_{22})$ diagram; (b) stress response in the$(\Sigma_{11}, \Sigma_{22})$ diagram; (c) isotropic part of stress response in the $(\Sigma_c, \varepsilon_c)$ diagram; (d) deviatoric part of the stress response in the $(q_\Sigma, q_\varepsilon)$ diagram.

Let us note that in our framework, we have chosen an octa-directional radial law with the consideration of eight preferred directions. For a better accuracy it would be better to extend this principle to a greater number of preferred directions. In that case, the method would remain exactly the same. However, if we consider the numerical implementation of the model, the number of preferred directions has an impact on the computation time. We found that

eight directions is a good compromise between the model accuracy, its relevance and the calculation time.

5. Exploitation and assessment of the constitutive model

The theoretical model presented in the last paragraphs was implemented in the finite element code ABAQUS using a fortran user routine (UMAT). In this section, we present an identification method of the model (see subsection 5.1). Then, we carry out the model validation through a comparison with experimental data (see subsection 5.2). Then, we present an example of calculation of a whole sail (see subsection 5.3). Finely, we propose a general discussion that summarizes the strengths and limitations of the model (see subsection 5.4).

5.1 Identification method

The proposed approach was mainly designed to be adapted to an individual identification of the behaviour of each component of material: warp yarns, weft yarns and coating. Thus, in order to identify the array of the model parameters, it is necessary to perform tests on the unbleached material before the coating operation (that we will call material A) and on the coated material (that we will call material B). The results of these tests and the comparison of the behaviour of the both materials enable an identification of the behaviour induced by the crimp and the interactions between the different components: between the yarns themselves (warp/weft) and between the yarns and the coating. The identification method of the model is presented in this subsection in three steps.

- **Step 1 : Tests on material A and identification of the yarns behaviour**

The identification of the yarns behaviour, characterized from Eq.(29) to Eq.(35), is performed with an identical procedure that we apply for the weft direction and for the warp direction of

the material. The tests that are necessary in this procedure are described on Fig. 15, where x denotes the loading direction ($x = a$ for warp direction and $x = e$ for weft direction).Two kinds of tests are required. The first test consists in performing a cyclic tensile test with several unloading-reloading cycles, controlled in strain or in stress for different values of ε_x^R. This test is interrupted with relaxation steps R_i (at constant strain) or with creep steps C_i (at constant stress). Fig.15-a and Fig.15-b give two illustrations of the obtained results of this kind of test with only one cycle. During this test, the creep and relaxation steps disclose the independent-time irreversible behaviour, corresponding with the stress $\Sigma_{x,h}(\varepsilon_x)$ (red color on Fig.15-a and Fig.15-b). Indeed, the viscous contribution $\Sigma_{x,v}(\dot{\varepsilon}_x)$ of the yarn behaviour has a fluid-type character (see Eq.(28), Eq.(29) and Fig.4)) and tends to vanish after a quite long relaxation or creep step. The evolution of the stress $\Sigma_{x,h}(\varepsilon_x)$ revealed in the end of creep or relaxation step enables to identify the parameters of the laws $\mathcal{L}_{x,1}(\varepsilon_x^R)$ and $\mathcal{L}_{x,2}(\Delta\varepsilon_x)$ defined by Eq.(32) and Eq.(33).

The second type of test is described by Fig.15-c. It enables the parameters identification of the viscous contribution $\Sigma_{x,v}(\dot{\varepsilon}_x)$ of the yarn behaviour, defined by Eq.(29) and Eq.(30). It is a matter of simple tensile tests with different strain rates. By knowing the expression of the law $\mathcal{L}_{x,1}(\varepsilon_x)$, identified with the first type of test, it is possible to deduce the evolution of the viscous component that corresponds with the stress difference : $\Sigma_x(\varepsilon_x, \dot{\varepsilon}_x) - \mathcal{L}_{x,1}(\varepsilon_x)$. Those curves present an initial elastic modulus K_x and saturation thresholds $S_i = \eta_x(\dot{\varepsilon}_{xi}).\dot{\varepsilon}_{xi}$, that enable the identification of the viscosity evolution as a function of the strain rate $\eta_x(\dot{\varepsilon}_{xi}) = S_i/\dot{\varepsilon}_{xi}$.

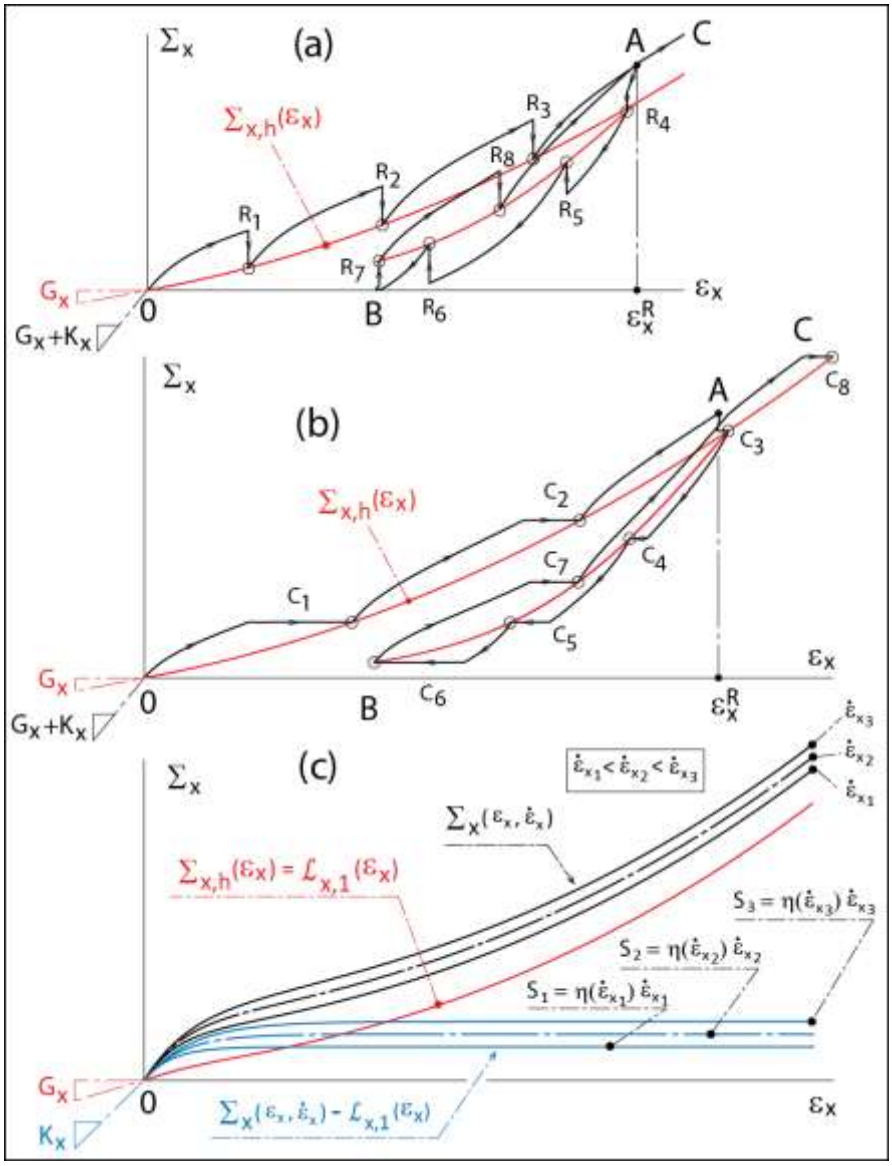

Fig.15. Identification of the behaviour of the yarns: (a) Cyclic tensile test 0ABAC interrupted with relaxation steps R_i ; (b) Cyclic tensile test 0ABAC interrupted with creep steps C_i ; (c) Simple tensile tests performed at different strain rates.

- **Step 2 - Off-axis test on material A and identification of the interaction between yarns behaviour**

The behaviour of the interaction between yarns, defined by Eq.(44) is difficult to characterize by a direct measure. In order to identify this behaviour, it is necessary to perform a 45° off-axis simple tensile test, on material A (Bias-extension test characterized by an angle $\theta = 45°$)

(see for instance, Wang et al. (1998) and King et al.(2005)). This test is then modelled through Eq.(26), knowing that for material A: $\underset{\sim}{\boldsymbol{\Sigma_c}} = \underset{\sim}{\mathbf{0}}$ and $\overline{\rho} = \overline{\rho}_f$. This is possible according to the step 1 that enables to identify the yarns behaviour in the warp direction Σ_a and the weft direction Σ_e. The comparison between the model response and the experimental bias-extension test results enables the characterization of the interaction between yarns behaviour, represented by Σ_i in Eq.(26) and defined by a linear elastic law in Eq.(44). The fig. 16 shows qualitatively the shape of the response of the material A during a bias-extension test, for two values of the elastic modulus K_γ.

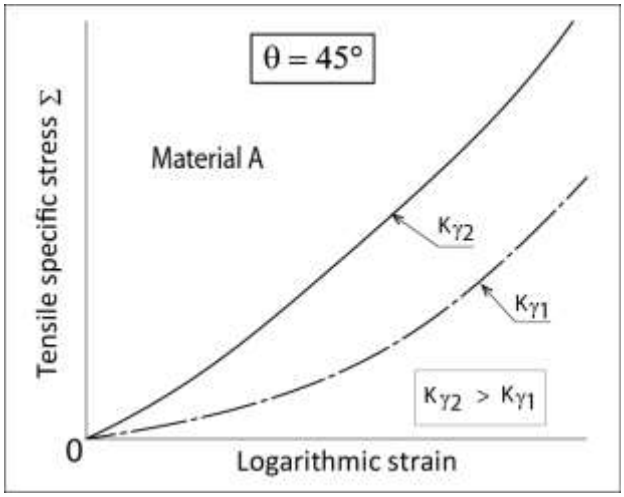

Fig.16. Qualitative illustration of the influence of the value of the elastic modulus K_γ on the shape of the response of the material A during a bias-extension test (see Eq.(44)).

- **Step 3 - Tests on material B and identification of the coating behaviour**

As in the case of the yarns, on Fig.15-a or on Fig.15-b, cyclic tensile tests interrupted by relaxation steps or by creep steps on the material B are necessary, in order to identify the time-independent behaviour of material B, in the warp or in weft directions (see Fig.17-a curve 1). In the warp and weft directions, this behaviour is composed of the time-independent behaviour of the yarns (see Fig.17-a curve 2) and of the time-independent behaviour of the

coating (see Fig.17-a curve 3). Thus, whether we consider the warp direction or the weft direction, the time-independent behaviour of the coating is obtained by the subtraction of the yarn time-independent behaviour from the material B time-independent behaviour, in the considered direction. This is illustrated on Fig. 17-a.The time-independent behaviour of the coating is characterized by three moduli E_1, E_2 and E_3. The definition of the coating time-independent behaviour is made with a constant Poisson ratio ν, as it is indicated by Eq.(59). This Poisson ratio ν is difficult to characterize by a direct measure. For this, it is necessary to compare the model response and the results of the contraction effects of the cyclic tensile tests interrupted by relaxation steps or by creep steps previously performed on material B and to adjust the value of ν.

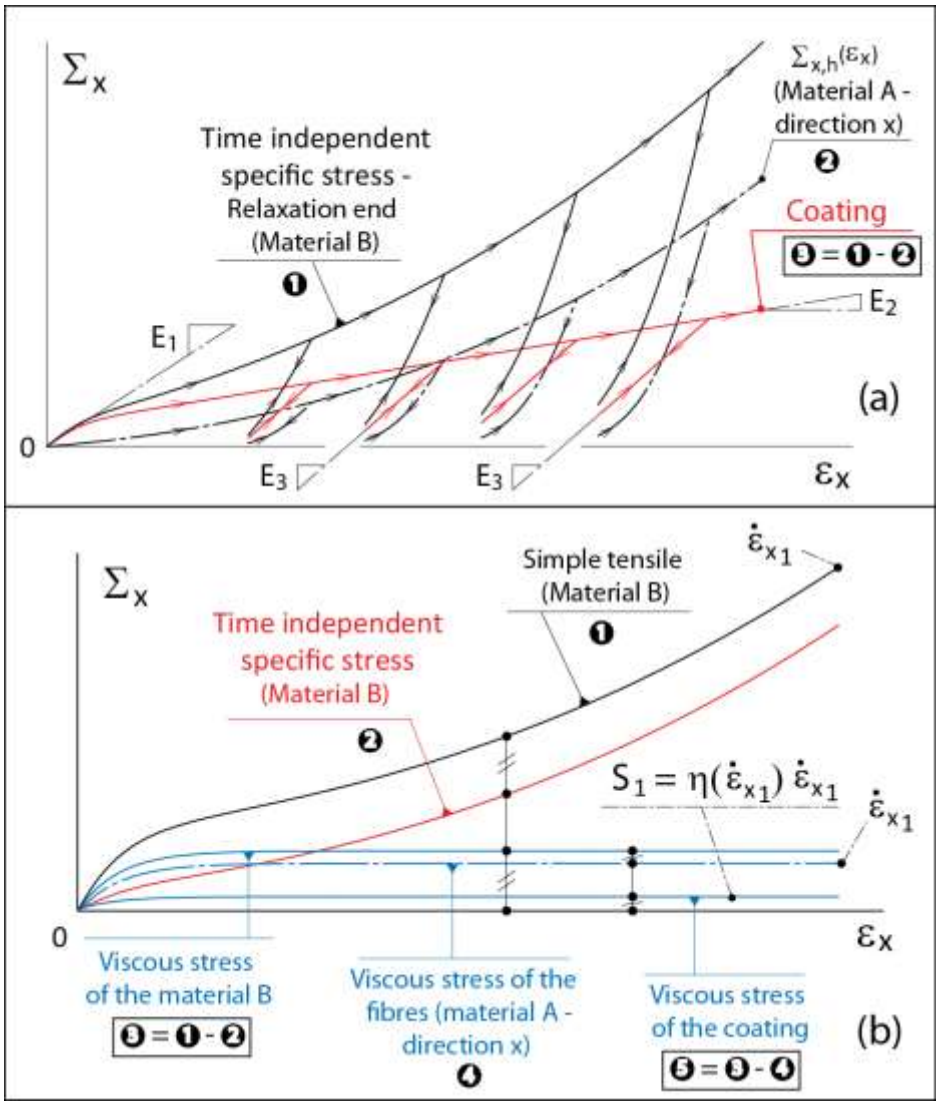

Fig.17. Identification of the behaviour of the coating: (a) time-independent behaviour (curve 3); (b) Viscous behaviour (curve 5).

Concerning the viscous behaviour of the coating, defined by Eq.(29), Eq.(30) and Eq.(46), the identification method is similar to the one introduced for the yarns (Fig.15-c). Indeed, the aim is to perform monotonous tensile tests at different strain rates, on material B. Fig.17-b describes the method of only one value of strain rate $\dot{\varepsilon}_{x1}$. By knowing the time-independent behaviour of material B (Fig.17-b curve 2), we can deduce, by subtraction, the viscous stress of material B (Fig.17-b curve 3). This effect takes into account the viscous behaviour of the yarns that is determined in the step 1 (Fig.17-b curve 4). Thus, the subtraction of the viscous effect of the yarns of the one of material B, enables to isolate the viscous stress of the coating (Fig.17-b curve 5). The comparison of the model predictions to the experimental measures of the saturation thresholds $S_i = \eta_x(\dot{\varepsilon}_{xi}).\dot{\varepsilon}_{xi}$ and the measure of the initial elastic modulus enables to identify the parameters of the Carreau-Yasuda law and the elastic moduli $\mathrm{K_c}$ and μ_v of the viscous contribution of the coating.

5.2. Model assessment according to experimental results

The validation of the modelling is made in this section by a confrontation of the model predictions to a set of experimental results, obtained from a woven material with polyester yarns and provided with a coating of polyester resin (see Dib (2014)). Measures and model identification for this material enabled to get the parameters values in appendix B. The whole description of the experimental results and the detailed identification procedure are beyond the scope of the current paper and will be the subjects of further presentations. A Comparison model-experiment for results of corrugated tensile test along the warp and weft directions is given in Fig.18. This test corresponds with a tensile test with several cycles triggered regularly and strain-controlled, at a constant strain rate of $5.10^{-4}s^{-1}$. The model gives good

results for the first loading and the unloading/reloading cycles, on Fig.18-a and 18-c. Fig.18-b and 18-d show that the material presents a stronger contraction effect for a tensile test along the weft direction. This effect, due to the crimp of warp yarns, is quite well reproduced by the model. Besides, the experimental results show a swelling phenomenon that occurs during a corrugated tensile phase in the warp direction, in the unloading/reloading steps aba, cdc and efe on Fig.18-b. This phenomenon that is quite unusual seems to be well reproduced by the model. Let us note that the experimental results and the modelling of the stress-controlled corrugated tensile tests do not show any swelling phenomenon.

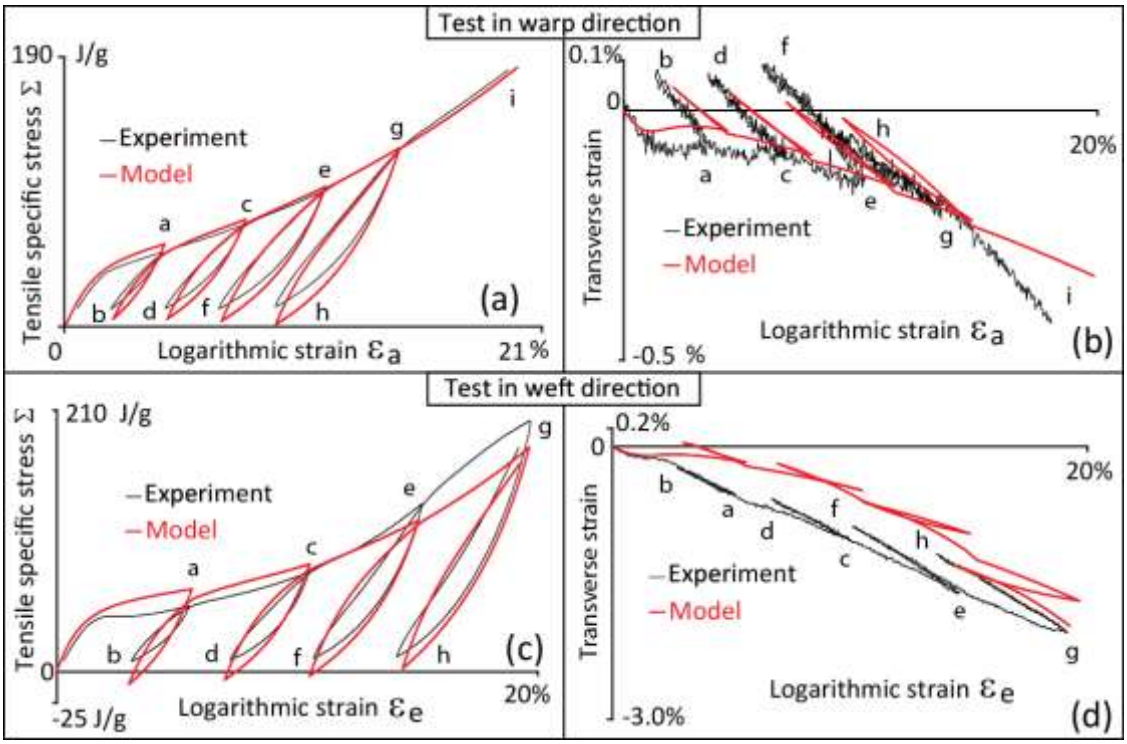

Fig. 18 :Comparison model-experiment for a corrugated tensile test along the warp direction(a and b) and weft direction (c and d) .Curves (a) and (c) give the stress as a function of axial strain and curves (b) and (d) give transverse strain as a function of axial strain, respectively in warp and weft directions.

Fig. 19 shows comparison between the model and the experimental results of monotonous strain-controlled tensile tests, with relaxations steps in the direction of warp yarns and weft

yarns. On Fig. 19-a and 19-c, the model remains satisfactory in reproducing the viscous behaviour of the material during the relaxation steps. According to the stiffness of the yarns in the weft direction, linked to their straight shapes, Fig.19-b shows that a tensile phase in the warp direction brings little contraction effect compared to the one in the weft direction on fig.19-d. These effects are well reproduced by the model.

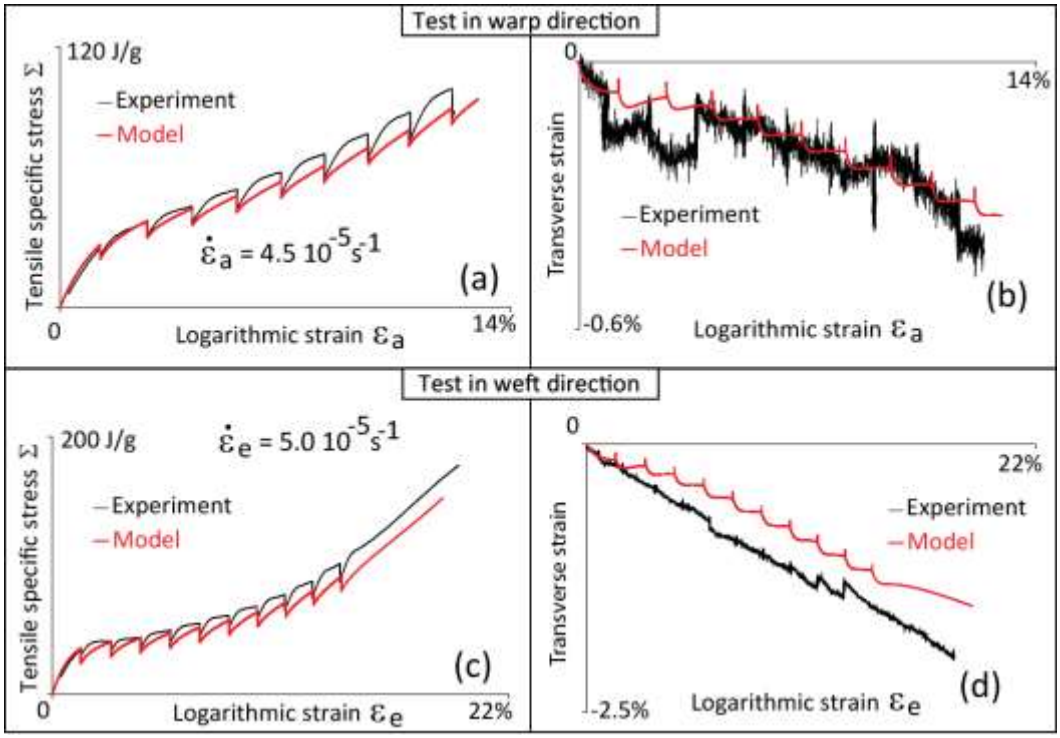

Fig. 19: Comparison model-experiment in monotonous tensile tests with relaxation steps in the direction of warp yarns (a and b) and weft directions (c and d).Curves (a) and (c) give the stress as a function of axial strain and curves (b) and (d) give transverse strain as a function of axial strain, respectively in warp and weft directions.

Fig. 20 shows a comparison between the model and the experimental results of off-axis tensile tests with different angles between the warp yarns and the tensile direction. Those tests were strain-controlled at a strain rate of for orientations and at a

strain rate of $10^{-3}s^{-1}$ for the orientation $\theta = 45°$. One can see that the model remains satisfactory in taking into account the anisotropic effects.

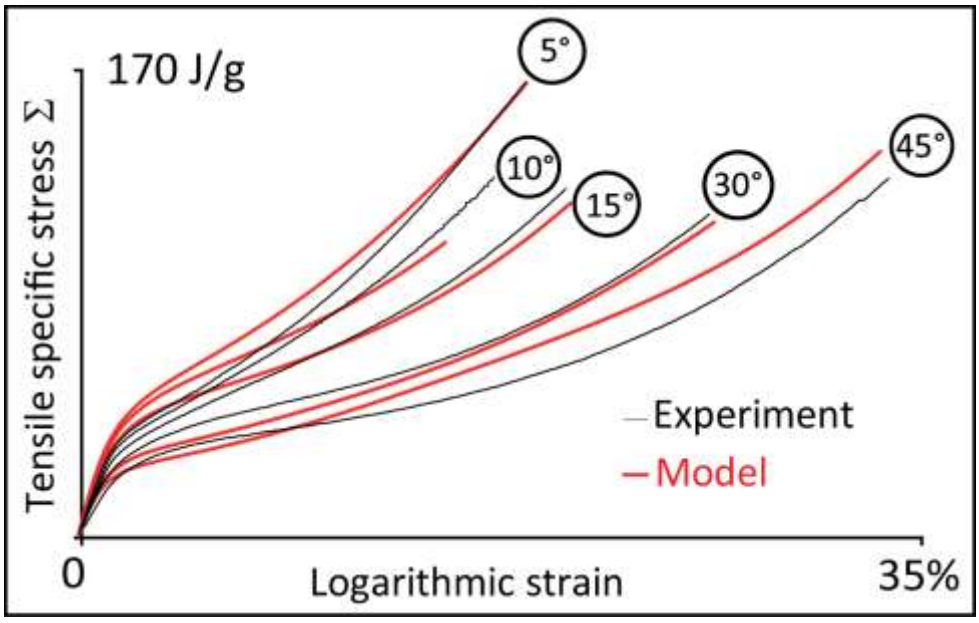

Fig. 20: Comparison between model and experiments in the case of off-axis tensile tests with different angles between the warp yarns and the tensile direction:

$\theta = 5°, 10°, 15°, 30°$ and $45°$.

Fig. 21 shows a simulation of an off-axis experiment ($\theta = 10°$) controlled at constant strain rate, with a complex loading including a simple unloading-loading ABA and a small cycle EFE in a bigger cycle CDC. Besides, this loading contains four relaxation steps noted R1 to R4. The test is performed with articulated clamps that enable a free rotation of the sample during loading. This rotation induced by the material distortion during loading discloses the anisotropic behaviour of the woven material. Fig.21-a shows the axial stress-strain curve. Fig.21-b shows the evolution of stress as a function of time, during the relaxation sequences. Fig. 21-c gives the evolution of the distortion angle with time. This angle is measured in the middle of the sample; it is denoted δ'; it is schematically illustrated on Fig. 21-c, by the distortion of a square initially drawn in the centre of the sample. Despite the complex loading,

the model gives good results. Fig. 21-a and 21-b show that increase or decrease of stress during a relaxation sequence is linked to the position of this latter in the cycle during the loading history. This viscous phenomenon is well predicted by the model. Moreover, Fig. 21-c shows that the model is able to capture accurately the evolution of the distortion angle δ' in the middle of the sample.

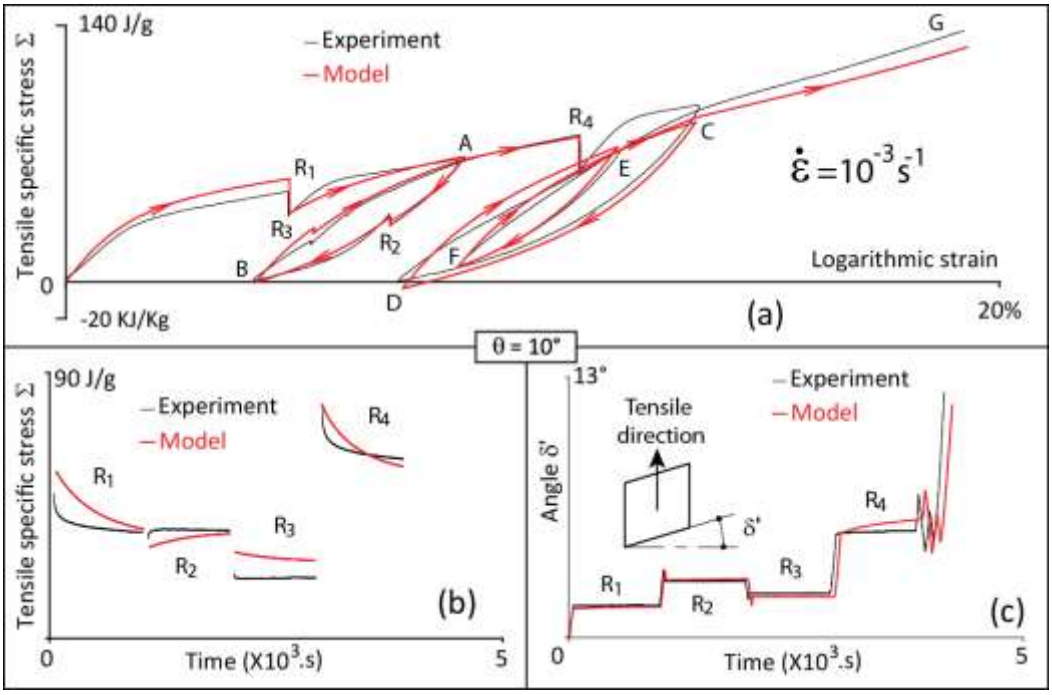

Fig. 21: Comparison between model and experiment in the case of an off-axis tensile test ($\theta = 10°$) with complex loading, containing relaxations and cycles: (a) stress as a function of strain, (b) evolution of stress as a function of time, during relaxation sequences, (c) evolution of the distortion angle δ', in the central part of the sample.

Fig. 22 gives comparison between model and experiment for a sinusoidal corrugated tensile test with a variable amplitude in the orientation of $\theta = 45°$. The loading program is given on Fig. 22-b. This test is force-controlled with a frequency of 0.3 Hz. The amplitude of the loading varies linearly as a function of time. The response of the material in strain is given on Fig. 22-a, in a stress-strain diagram. Fig. 22-c gives the evolution during the test of the

distortion angle δ, measured on the sample at the level of the articulated clamp as a function of the displacement. Let us note that the measure of the angle δ was realized only during the six first cycles. The model predicts accurately the behaviour on Fig. 22-a. Fig. 22-c shows that the model overestimates the displacement; this is linked to a weaker stiffness than in reality, during the beginning of the test. However, the prediction of the distortion angle δ value is correct.

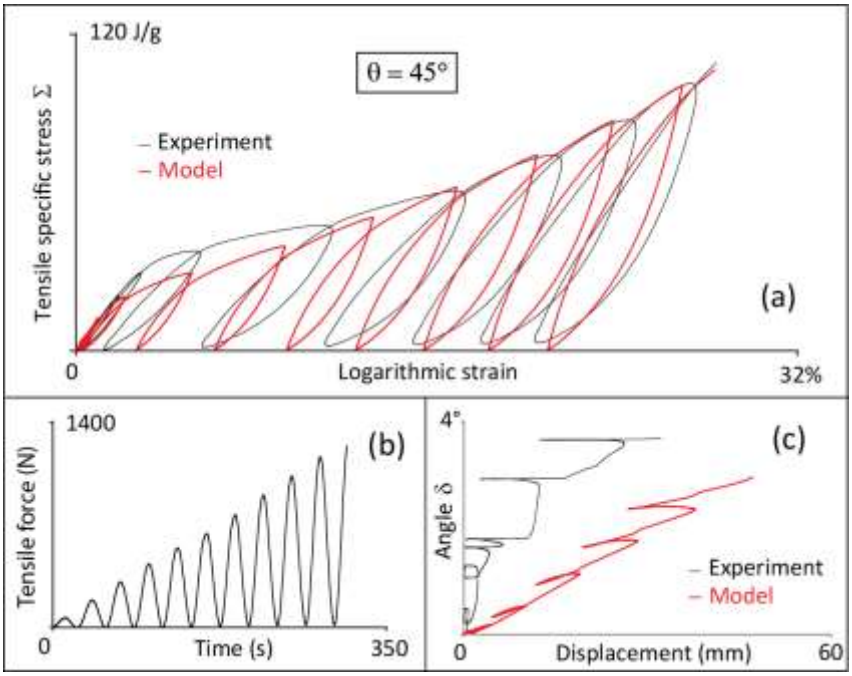

Fig. 22: Comparison model-experiment in the case of a bias test controlled in force: (a) stress as a function of axial strain, (b) evolution of tensile force imposed during the test, (c) evolution of the distortion angle δ, at the level of the articulated clamp of the sample.

Fig.23 gives some results of modelling of a bias-extension test. In order to discuss these results, we distinguish the stress due to the yarns, the interaction between the yarns and the coating, and we adopt a particular notation for each of those stress contributions. The total stress tensor defined by the equation (26) can be considered as the sum of three tensors: $\underset{\sim}{\boldsymbol{\Sigma}} = \underset{\sim}{\boldsymbol{\Sigma_1}} + \underset{\sim}{\boldsymbol{\Sigma_2}} + \underset{\sim}{\boldsymbol{\Sigma_3}}$. The first tensor stands for the yarns behaviour: $\underset{\sim}{\boldsymbol{\Sigma_1}} = \frac{\overline{\rho}_a}{\overline{\rho}} \Sigma_a (\vec{u} \otimes \vec{u}) +$

$\frac{\overline{\rho}_e}{\overline{\rho}}\Sigma_e(\vec{v}\otimes\vec{v})$; the second tensor stands for the interaction between yarns: $\underset{\sim}{\boldsymbol{\Sigma_2}} = \frac{\overline{\rho}_f}{\overline{\rho}}\Sigma_i(\vec{u}^*\otimes\vec{v} + \vec{v}^*\otimes\vec{u})$ and the third tensor stands for the coating: $\underset{\sim}{\boldsymbol{\Sigma_3}} = \frac{\overline{\rho}_c}{\overline{\rho}}\underset{\sim}{\Sigma_c}$. We can also distinguish the stress tensor linked to weaving, denoted by $\underset{\sim}{\boldsymbol{\Sigma_f}}$, such as: $\underset{\sim}{\boldsymbol{\Sigma_f}} = \underset{\sim}{\boldsymbol{\Sigma_1}} + \underset{\sim}{\boldsymbol{\Sigma_2}}$. During the bias tensile test, the total stress component Σ, along the tensile axis, is the sum of three components, denoted Σ_1, Σ_2 and Σ_3 corresponding respectively to the three tensors previously introduced $\Sigma = \Sigma_1 + \Sigma_2 + \Sigma_3$. Besides, we denote by $\Sigma_f = \Sigma_1 + \Sigma_2$ the component along the tensile axis of the stress tensor linked to the weaving. Figure 23-a gives a comparison of the total stress obtained in a bias tensile test and its modeling, and on the other hand, the evolution of the total modeled stress is divided into three contributions: the stress Σ_1 due to the yarns, the stress Σ_2 due to the interaction of the yarns and stress Σ_3 due to the coating. This figure shows a relatively complex coupling effect between the different stress contributions. Indeed, this coupling is manifested, for example, by a non-linear behaviour of the stress Σ_2 related to the interaction between the yarns, despite the linear law adopted (see Eq. (44)). Fig. 23-b shows the evolution of the angle α between the warp yarns and the weft yarns. At the end of the test, the measured angle α = 54.4 °, the value foreseen by the model is α = 53.5 ° (error of 1.6%). Note that the test ends with the fracture of the sample at a deformation of 33.8%, which leads to a maximum value of the angle of distortion (or shear angle) γ = 36.6 °. This value is much lower than the value of the shear-locking angle obtained by Boisse et al (2006): γ = 0.9 rd = 51.6 °. This result reinforces the relatively simple approach adopted by the hypothesis of Eq.(44). Fig. 23-c gives the results of modelling of the same test, under the same conditions as Fig. 23-a, with in addition a relaxation R of 300 s and an ABA cycle. This figure gives the evolutions of the stress Σ_f due to the weaving and the stress Σ_3 due to the coating. This result shows that the coupling effects lead to a viscous behaviour of the weaving, in spite of the relatively simple law adopted for the interaction of

the yarns (see Eq. (44)). Figure 23-d shows the stress Σ_f due to the weaving, obtained in Figure 23-c and the evolution 0A' of stress Σ of the monotonous response of the material without coating (unbleached material), which undergoes the same strain rate. This result shows the importance of the coupling effects on the overall behavior of the material and more precisely the effect of the coating on the weaving behaviour.

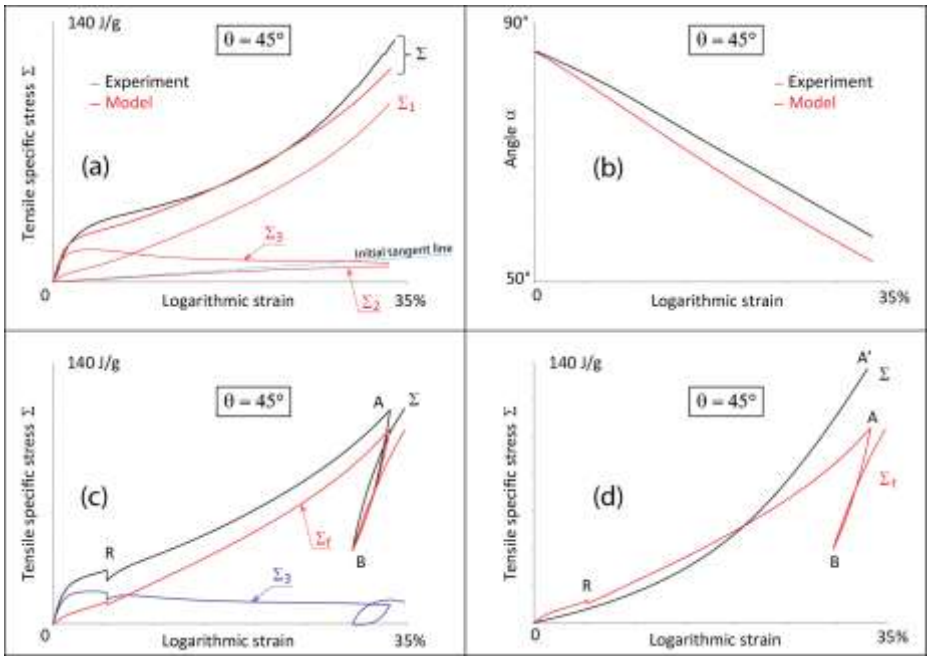

Fig. 23: Modelling of a bias-extension test, were strain-controlled at a strain rate of $10^{-3}s^{-1}$: (a) model-experiment comparison of the response of total stress Σ and evolutions of stress Σ_1 due to yarns, Σ_2 due to the yarns interaction and Σ_3 due to the coating, such as: $\Sigma = \Sigma_1 + \Sigma_2 + \Sigma_3$; (b) evolution of the angle α between warp and weft yarns ; (c) modelling results of the same test in the same conditions as the fig. 23-a, with a relaxation R of 300s and an ABA cycle and evolution of stress $\Sigma_f = \Sigma_1 + \Sigma_2$ due to the weaving and stress Σ_3 due to the coating ; (d) comparison of the evolution 0RABA of stress Σ_f due to weaving obtained of the fig. 23-c and evolution 0A' of stress Σ of the monotonous response of the material without coating (unbleached material) that undergoes the same strain rate.

Fig. 24-a gives a comparison model-experiment in the case of sinusoidal corrugated tensile test, in the weft direction, with a frequency of 0.3 Hz, stress-controlled between stress at point A and stress at point B. Fig. 24-a shows an effect of ratcheting of the cycles in strain in direction AC. The model captures satisfactorily this phenomenon. Indeed, the model reproduces a fast ratchet effect at the beginning of cycle, which then presents a saturation sequence. Nevertheless, the model overestimates the final position of the cycle with an error of the order of 10% of the calculated value. This is related to the difference in rigidity between the model and the reality before the cycle begins at point A. Fig. 24-b gives a comparison model-experiment during a monotonous tensile test OA, in the warp direction, controlled at a strain rate of . This sequence is completed at point A by a sinusoidal loading of frequency 0.1 Hz, strain-controlled, between strain at point A and strain at point B. Fig. 24-b shows an effect of crawling of the cycles in stress in direction AC. The model is also able to capture satisfactorily this phenomenon. Indeed, the model predicts with very good accuracy the final stress value of the cycle, as well as a rapid progression effect at the beginning of cycling and saturation at the end. Note that this result is obtained despite a small shift in the strain control at points A and B between experiment and modeling.

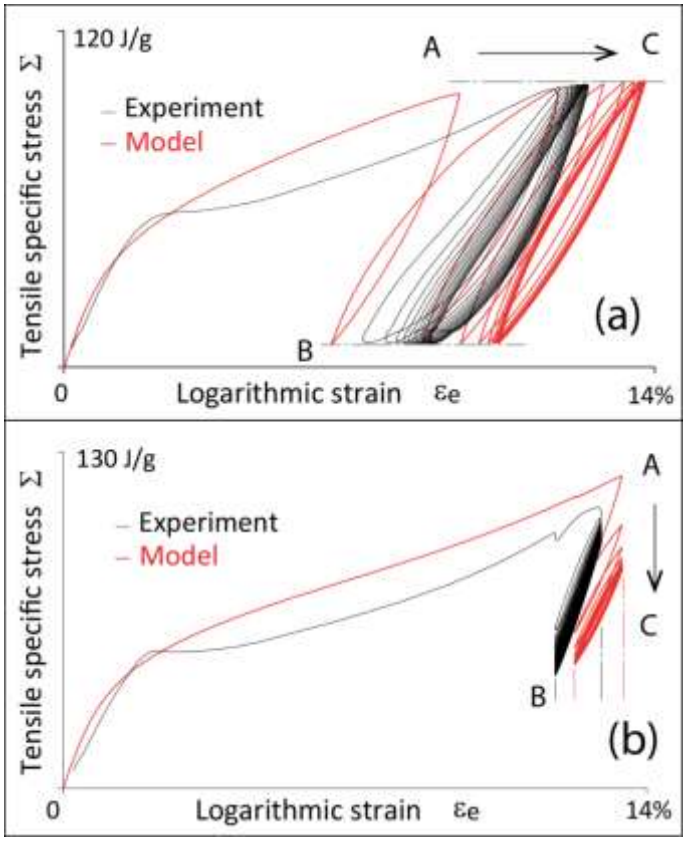

Fig. 24: Corrugated tensile test in the weft direction: (a) stress control, (b) strain control.

5.3. Application on a sail structure

We present in this section, the results of the calculation of a whole sail thanks to the code ABAQUS. We consider the woven material with polyester yarns provided with a coating in polyester resin, studied in the previous subsection and whose parameters are defined in Appendix B. Fig. 25-a defines the sail geometry that is composed of different flat panels caracterized by the initial orientation θ_0 of their warp yarns. The head point, the clew point and the tack point present multi-layers lining of the same material whose the orientation θ_0 is defined as a function of the color of the reinforcement, on Fig. 25-a and varies from 5° to 90°. The leech of the sail is 13 m, its foot measures 5.65 m and its luff is 14.75 m long. Along the luff, the sail is provided with an unistrand steel cable whose the diameter is 10 mm.

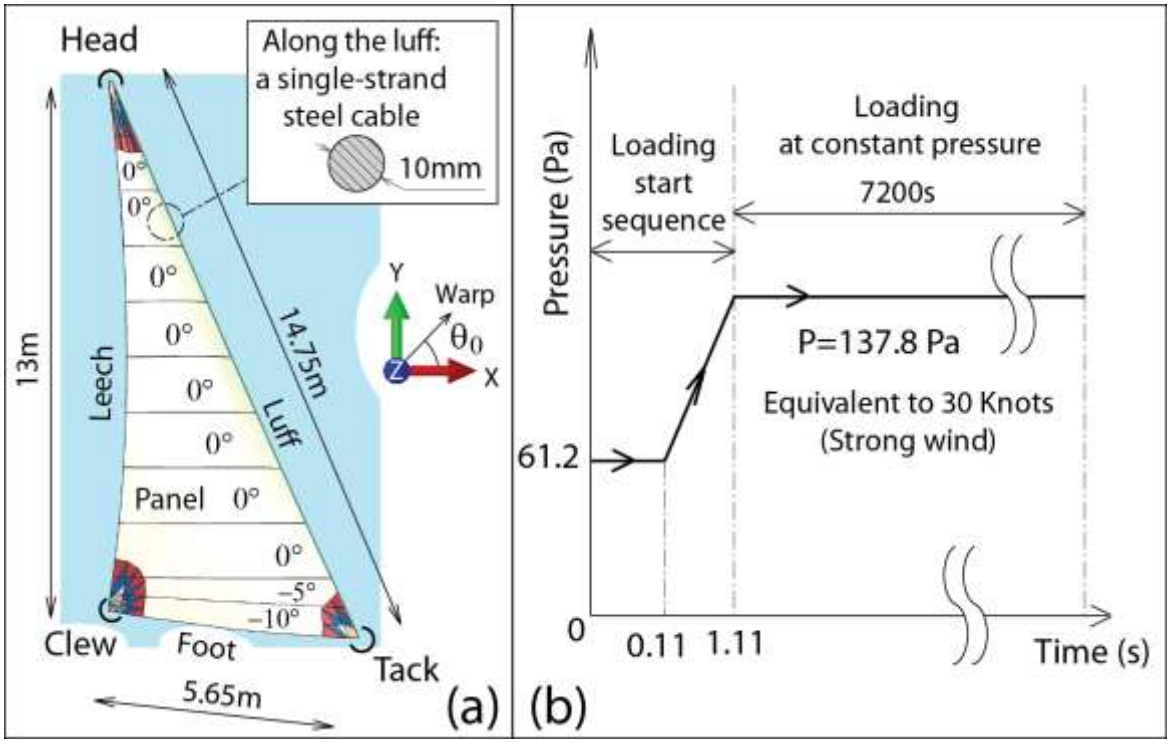

Fig. 25 : Definition of : (a) the sail geometry and (b) the loading history.

The loading adopted for the sail is defined on Fig. 25-b. This loading is equivalent to a 2-hour sailing in conditions of strong wind at a constant pressure P=137.8Pa. The cruise pressure is reached after a fast increase from a first plateau of pressure at P=61.2 Pa (duration: 0.11 s), followed by a controlled increase to the cruise pressure during 1 s. For the mesh of the sail, we adopted membrane triangular elements with three nodes (see Fig.26). For the modelling of the steel cable along the luff, we chose bar elements with two nodes. The boundary conditions of the sails are defined on Fig. 26: we imposed a null displacement $(\vec{U} = \vec{0})$ at the head point, at the clew point and at the tack point, renamed respectively points 0_1, 0_2 and 0_3.

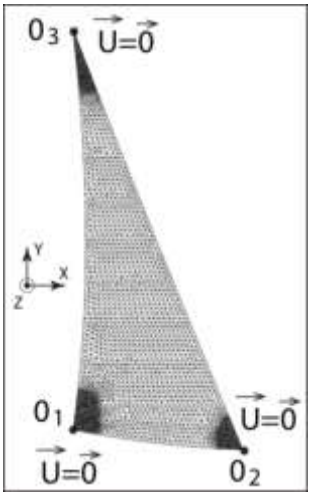

Fig. 26: Mesh and boundary conditions for the sail.

Fig. 27-a gives a result of specific stress in weft yarns. Fig. 27-b gives a result of the displacements calculation along the z-axis. This figure shows that the maximal displacement is located along the leech of the sail around the point A and presents a value close to 380 mm. Fig. 27-c gives a qualitative information of the sail deformation and a comparison between its final and initial shapes.

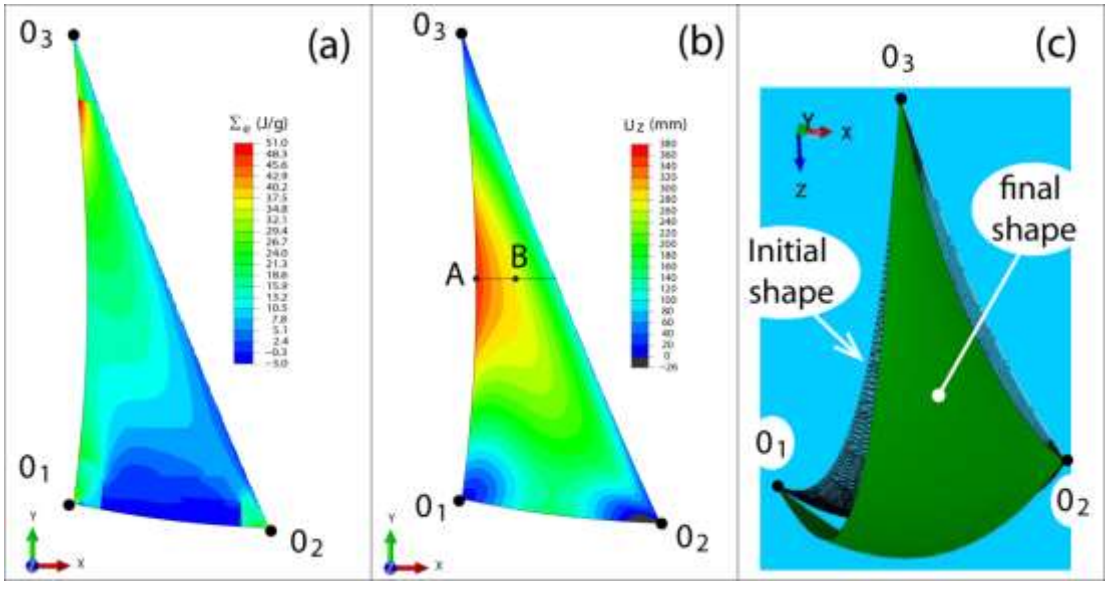

Fig.27: Results of the calculation of the sail: (a) Specific stress in weft yarns, (b) displacement along the z-axis (perpendicularly to the figure plane), (c) comparison between the initial and final shapes of the sail.

We now focus on points A and B defined in Fig. 27-b. Fig. 28-a and 28-b give the evolution during the loading history of the first invariant and of the radius in the deviatoric plane, respectively, of the strain and specific stress, at points A and B. The sail loading with a constant pressure could be assimilated to a simple creep-type solicitation. Nevertheless, the results of the Fig. 28-a and 28-b show complex evolutions of the invariants of stress and strain, that do not correspond to a creep-type solicitation.

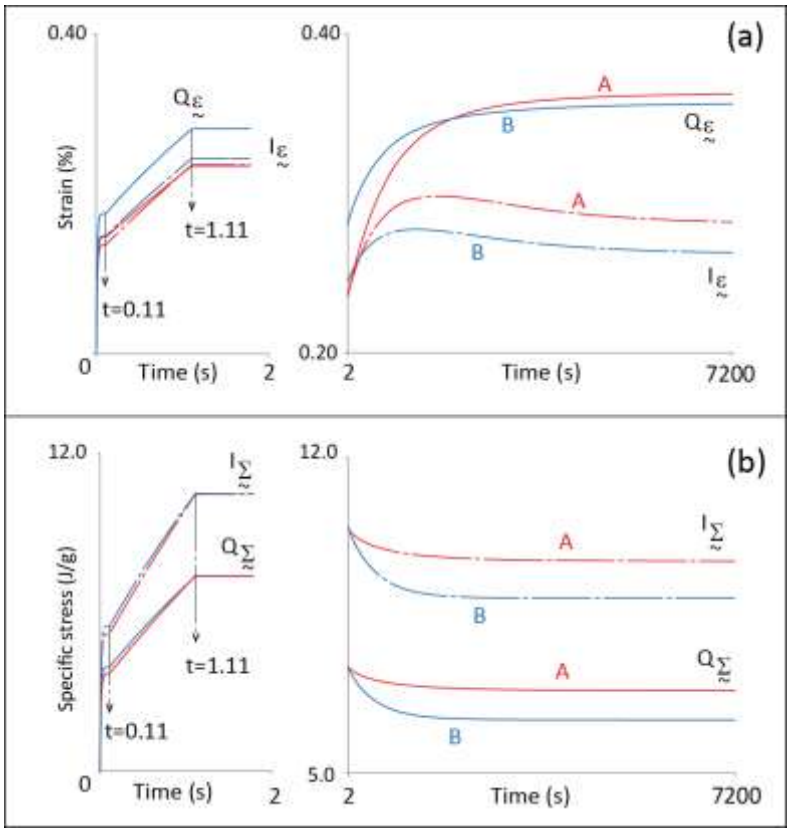

Fig.28: Evolution of strain and specific stress during loading at points A and B of the sail, defined on Fig. 27-b: (a) Evolution of the first invariant and of the radius in the deviatoric plane of strain, (b) Evolution of the first invariant and of the radius in the deviatoric plane of specific stress.

This conclusion is confirmed by Fig. 29 that gives in a specific stress-strain diagram, the evolution of the first invariant of stress as a function of the first invariant of strain $I_{\underset{\sim}{\boldsymbol{\Sigma}}}(I_{\underset{\sim}{\boldsymbol{\varepsilon}}})$ and also, the evolution of the radius in the deviatoric plane of stress as a function of the radius in the deviatoric plane of strain $Q_{\underset{\sim}{\boldsymbol{\Sigma}}}(Q_{\underset{\sim}{\boldsymbol{\varepsilon}}})$. Indeed, this result shows a complex evolution of the sail response to the constant pressure loading, that does not correspond to a creep-type loading at all.

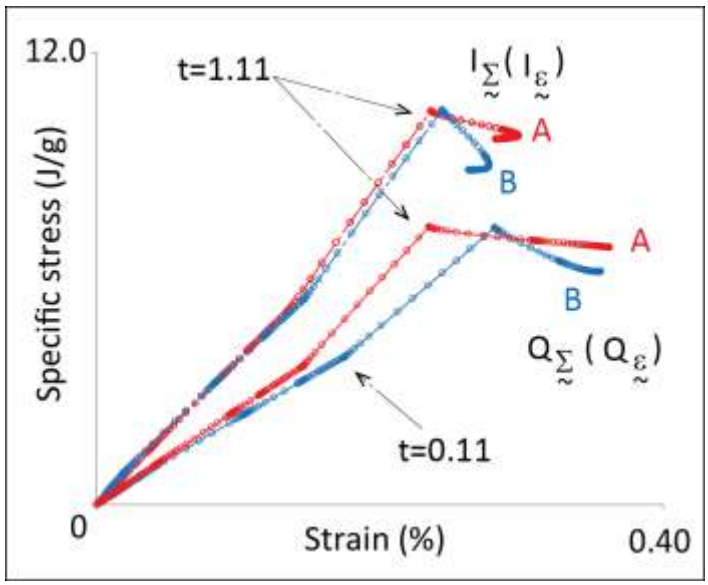

Fig. 29: Specific stress - strain diagram, at points A and B of the sail, defined on Fig. 27-b : Evolution of the first invariant of stress as a function of the first invariant of strain $I_{\underset{\sim}{\boldsymbol{\Sigma}}}(I_{\underset{\sim}{\boldsymbol{\varepsilon}}})$ and evolution of the radius in the deviatoric plane of stress as a function of the radius in the deviatoric plane of strain $Q_{\underset{\sim}{\boldsymbol{\Sigma}}}(Q_{\underset{\sim}{\boldsymbol{\varepsilon}}})$.

5.4. General discussion

In its present version, the range of validity of the model is limited to the family of materials for which the value of the distortion angle remains low compared to shear-locking angle, even

for loads close to the rupture of the material, which is described by a linear law to model the interaction behaviour between warp an weft yarns, at a binding point.

In addition, the developed approach is based on equations (24) and (25), which are fundamental assumptions, that give to our approach, a phenomenological character. As a result, the woven material is considered as continuum medium, endowed with particular properties. Thus, our approach does not take into account neither damage to material by mechanical loading nor the sliding between the yarns and coating nor the sliding between the yarns.

However, the model deals simultaneously with the non-Newtonian viscous behaviour, the time-independent irreversibility, the anisotropy and the cyclic loading behaviour of coated woven fabric. The model takes also into account the angle variation between warp and weft yarns, the individual behaviours of the warp and weft yarns, the coating and their interactions.

The modeling approach proposed in this study is relatively promising. The model obtained is an interesting investigative tool for studying the behaviour of coated and uncoated woven materials, as well as yarns-yarns and yarns-coating couplings.

6. Conclusion

An original approach of modelling of the mechanical behaviour of coated woven materials has been proposed. This modelling deals simultaneously with the non-Newtonian viscous behaviour, the time-independent irreversibility, the anisotropy and the cyclic loading behaviour of coated woven fabric. The proposed model takes into account the individual behaviours of the warp yarns, the weft yarns, the coating and their interactions. The model takes also into account the angle variation between warp and weft yarns. The proposed model

has been implemented in the finite element code ABAQUS using a fortran user routine (UMAT). The model has been validated by a comparison of its response to experimental results on a woven material with polyester yarns and provided with a coating of polyester resin. This confrontation has shown promising results concerning the forecast of the cyclic behaviour, of the Poisson contraction effects during simple tensile tests, of the viscous behaviour, of the anisotropic effects of the behaviour, of the ratchet effects in stress and in strain. At last, an example of calculation of a complete sail structure has been presented. This calculation has shown a complex response of the sail material, and a non-negligible strain due to the material viscosity, despite a relatively simple loading at constant pressure.

Appendix A: Representation space of a symmetric 2D tensor

Let us consider a symmetric 2D tensor $\underset{\sim}{\boldsymbol{A}}$, defined in a point *P* of a woven material, in the fixed reference orthonormal frame $(\overrightarrow{e_1},\overrightarrow{e_2})$, such as :

$$\underset{\sim}{\boldsymbol{A}} = \begin{pmatrix} A_{11} & A_{12} \\ A_{12} & A_{22} \end{pmatrix}_{(\overrightarrow{e_1},\overrightarrow{e_2})} \qquad \text{(A.1)}$$

The first invariant and the deviatoric tensor, written respectively $I_{\underset{\sim}{\boldsymbol{A}}}$ and $\underset{\sim}{\overline{\boldsymbol{A}}}$, are such as:

$$I_{\underset{\sim}{\boldsymbol{A}}} = Tr\left(\underset{\sim}{\boldsymbol{A}}\right) \;\; ; \;\; \underset{\sim}{\overline{\boldsymbol{A}}} = \underset{\sim}{\boldsymbol{A}} - \frac{1}{2} I_{\underset{\sim}{\boldsymbol{A}}}.\underset{\sim}{\boldsymbol{I}} \quad \text{and} \quad \underset{\sim}{\overline{\boldsymbol{A}}} = \begin{pmatrix} q_{\underset{\sim}{\boldsymbol{A}}} & A_{12} \\ A_{12} & -q_{\underset{\sim}{\boldsymbol{A}}} \end{pmatrix}_{(\overrightarrow{e_1},\overrightarrow{e_2})} \qquad \text{(A.2)}$$

where $\underset{\sim}{\boldsymbol{I}}$ is the 2D identity tensor and $q_{\underset{\sim}{\boldsymbol{A}}}$ is such as:

$$q_{\underset{\sim}{\boldsymbol{A}}} = \frac{A_{11}-A_{22}}{2} \qquad \text{(A.3)}$$

The second invariant of the deviatoric tensor, written $II_{\underset{\sim}{\overline{\boldsymbol{A}}}}$, is such as:

$$II_{\underset{\sim}{\overline{\boldsymbol{A}}}} = Tr\left(\underset{\sim}{\overline{\boldsymbol{A}}}.\underset{\sim}{\overline{\boldsymbol{A}}}\right) = 2\left(q_{\underset{\sim}{\boldsymbol{A}}}{}^2 + A_{12}{}^2\right) \geq 0 \qquad \text{(A.4)}$$

One can define the radius in the deviatoric plane, written $Q_{\underset{\sim}{\boldsymbol{A}}}$, such as:

$$Q_{\underset{\sim}{\boldsymbol{A}}} = \sqrt{II_{\underset{\sim}{\overline{\boldsymbol{A}}}}} = \sqrt{2}\left(q_{\underset{\sim}{\boldsymbol{A}}}{}^2 + A_{12}{}^2\right)^{1/2} \qquad \text{(A.5)}$$

The tensor $\underset{\sim}{\boldsymbol{A}}$ can be represented by a vector$\vec{A}$, in a representation space, such as:

$$\vec{A} = A_{11}.\overrightarrow{a_1} + A_{22}.\overrightarrow{a_2} + \sqrt{2}.A_{12}.\overrightarrow{a_3} \qquad \text{(A.6)}$$

where, $(\overrightarrow{a_1},\overrightarrow{a_2},\overrightarrow{a_3})$ is an orthonormal basis of the symmetric 2D tensor space (fig. A.1). Thus, the scalar product $\vec{A}.\vec{B}$ is defined by:

$$\vec{A}.\vec{B} = Tr\left(\underset{\sim}{\boldsymbol{A}}.\underset{\sim}{\boldsymbol{B}}\right) \qquad \text{(A.7)}$$

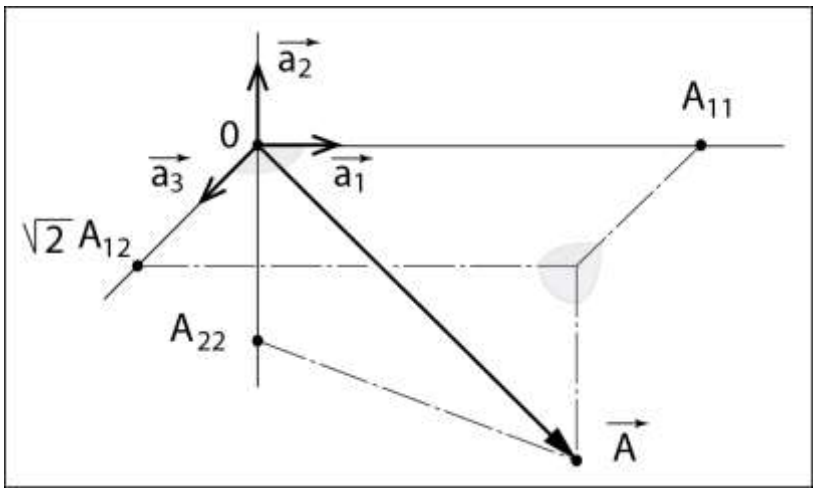

Fig.A.1: Representation of the tensor $\underset{\sim}{\boldsymbol{A}}$ by a vector $\vec{A}$ of coordinates$(A_{11}, A_{22},\sqrt{2}A_{12})$ in the base $(\overrightarrow{a_1},\overrightarrow{a_2},\overrightarrow{a_3})$ of the representation space.

According to Eq.(A.2), the tensor $\underset{\sim}{\boldsymbol{A}}$ can be written:

$$\underset{\sim}{\boldsymbol{A}} = \frac{1}{2} I_{\underset{\sim}{\boldsymbol{A}}}.\begin{pmatrix}1 & 0\\ 0 & 1\end{pmatrix}_{(\overrightarrow{e_1},\overrightarrow{e_2})} + q_{\underset{\sim}{\boldsymbol{A}}}.\begin{pmatrix}1 & 0\\ 0 & -1\end{pmatrix}_{(\overrightarrow{e_1},\overrightarrow{e_2})} + A_{12}.\begin{pmatrix}0 & 1\\ 1 & 0\end{pmatrix}_{(\overrightarrow{e_1},\overrightarrow{e_2})} \qquad \text{(A.8)}$$

One can introduce the tensors $\underset{\sim}{\boldsymbol{I}}$, $\underset{\sim}{\boldsymbol{J}}$ and $\underset{\sim}{\boldsymbol{K}}$ such as:

$$\underset{\sim}{\boldsymbol{I}} = \begin{pmatrix}1 & 0\\ 0 & 1\end{pmatrix}_{(\overrightarrow{e_1},\overrightarrow{e_2})}; \quad \underset{\sim}{\boldsymbol{J}} = \begin{pmatrix}1 & 0\\ 0 & -1\end{pmatrix}_{(\overrightarrow{e_1},\overrightarrow{e_2})}; \quad \underset{\sim}{\boldsymbol{K}} = \begin{pmatrix}0 & 1\\ 1 & 0\end{pmatrix}_{(\overrightarrow{e_1},\overrightarrow{e_2})} \qquad \text{(A.9)}$$

According to Eq. (A.6), those tensors are represented in the space, respectively, by the three vectors $\vec{I}$, $\vec{J}$ and$\vec{K}$, such as:

$$\vec{I} = \begin{pmatrix} 1 \\ 1 \\ 0 \end{pmatrix}_{(\vec{a_k})} ; \qquad \vec{J} = \begin{pmatrix} 1 \\ -1 \\ 0 \end{pmatrix}_{(\vec{a_k})} ; \qquad \vec{K} = \begin{pmatrix} 0 \\ 0 \\ \sqrt{2} \end{pmatrix}_{(\vec{a_k})} \qquad \text{(A.10)}$$

Therefore the vector $\vec{A}$ can be written:

$$\vec{A} = \frac{1}{2} I_{\underset{\sim}{A}} . \vec{I} + q_{\underset{\sim}{A}} . \vec{J} + A_{12} . \vec{K} \qquad \text{(A.11)}$$

The modulus of the vectors $\vec{I}, \vec{J}$ and $\vec{K}$, written I, J and K are :

$$I = \sqrt{Tr(\underset{\sim}{\boldsymbol{I}} . \underset{\sim}{\boldsymbol{I}})} = \sqrt{2}; \; J = \sqrt{Tr(\underset{\sim}{\boldsymbol{J}} . \underset{\sim}{\boldsymbol{J}})} = \sqrt{2} \; ; K = \sqrt{Tr(\underset{\sim}{\boldsymbol{K}} . \underset{\sim}{\boldsymbol{K}})} = \sqrt{2} \qquad \text{(A.12)}$$

Besides,

$$\vec{I} . \vec{J} = 0; \qquad \vec{I} . \vec{K} = 0 \; ; \qquad \vec{J} . \vec{K} = 0 \qquad \text{(A.13)}$$

Consequently, $(\vec{I}, \vec{J}, \vec{K})$ is an orthogonal basis in the representation space. Figure A.2 shows a geometric interpretation of Eq. (A.11) to Eq. (A.13), where the vector $\vec{I}$ is along the hydrostatic axis, and the vectors $\vec{J}$ and $\vec{K}$ are the basis vectors of the deviatoric plane.

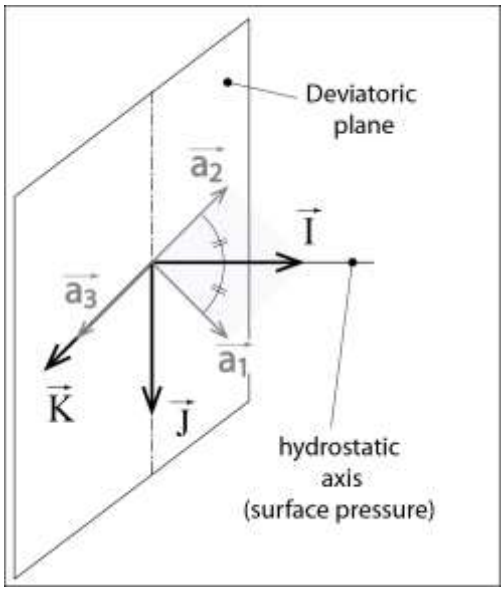

Fig.A.2 : Basis$(\vec{I}, \vec{J}, \vec{K})$ and geometric interpretation of the representation space.

The vector $\vec{A}$ of coordinates $(\frac{1}{2}I_{\underset{\sim}{A}}, q_{\underset{\sim}{A}}, A_{12})$ in the basis $(\vec{I},\vec{J},\vec{K})$ can be decomposed in a vector $\underline{\vec{A}}$ and a vector $\overrightarrow{OH}$, such as :

$$\vec{A} = \overrightarrow{OH} + \underline{\vec{A}} \quad , \text{ where } \overrightarrow{OH} = \frac{1}{2}I_{\underset{\sim}{A}}.\vec{I} \quad \text{and} \quad \underline{\vec{A}} = q_{\underset{\sim}{A}}.\vec{J} + A_{12}.\vec{K} \qquad \text{(A.14)}$$

The vector $\overrightarrow{OH}$ stands for the isotropic part of the tensor $\underset{\sim}{\boldsymbol{A}}$ and the vector $\underline{\vec{A}}$ stands for its deviatoric part. The modulus $\underline{A}$ of the vector $\underline{\vec{A}}$, corresponds to the radius in the deviatoric plane, indeed :

$$\underline{A} = \left(\underline{\vec{A}}.\underline{\vec{A}}\right)^{1/2} = \left\{Tr\left(\underset{\sim}{\boldsymbol{A}}.\underset{\sim}{\boldsymbol{A}}\right)\right\}^{1/2} = Q_{\underset{\sim}{A}} \qquad \text{(A.15)}$$

The location of vector $\underline{\vec{A}}$, in the deviatoric plane, can be defined by an orientation vector $\vec{u}_{\underset{\sim}{A}}$, such as :

$$\underline{\vec{A}} = Q_{\underset{\sim}{A}}.\vec{u}_{\underset{\sim}{A}} \qquad \text{(A.16)}$$

Eq.(A.14) and Eq. (A.16) can give the expression of the vector $\vec{u}_{\underset{\sim}{A}}$ as follows :

$$\vec{u}_{\underset{\sim}{A}} = \frac{q_{\underset{\sim}{A}}}{Q_{\underset{\sim}{A}}}.\vec{J} + \frac{A_{12}}{Q_{\underset{\sim}{A}}}.\vec{K} \qquad \text{(A.17)}$$

The vector $\vec{u}_{\underset{\sim}{A}}$ is an unit vector, indeed, its modulus written $u_{\underset{\sim}{A}}$ is such as:

$$u_{\underset{\sim}{A}} = \left(\vec{u}_{\underset{\sim}{A}}.\vec{u}_{\underset{\sim}{A}}\right)^{1/2} = \frac{2{q_{\underset{\sim}{A}}}^2 + 2{A_{12}}^2}{{Q_{\underset{\sim}{A}}}^2} = 1 \qquad \text{(A.18)}$$

The radius in the deviatoric plane $Q_{\underset{\sim}{A}}$ is a positive scalar that can be seen as a deviatoric intensity of the tensor $\underset{\sim}{\boldsymbol{A}}$. Thus, Eq. (A.16) shows that the deviatoric tensor $\overline{\underset{\sim}{\boldsymbol{A}}}$ can be represented in the deviatoric plane, by its intensity $Q_{\underset{\sim}{A}}$ and its orientation $\vec{u}_{\underset{\sim}{A}}$.

Appendix B: Modelling parameters of a woven material in polyester yarns **provided with a coating in polyester resin.**

The initial mass per unit surface of respectively, the w**a**rp yarns, the w**e**ft yarns and the **c**oating are:

$$\overline{\rho}_a = 63\ g/m^2,\ \overline{\rho}_e = 105\ g/m^2 \text{ and } \overline{\rho}_c = 138\ g/m^2 \qquad \text{(B.1)}$$

The values of the identified model parameters for the material are given in the tables B.1 and B.2.

Designation	Parameter	Value	Unit
Time-independant irreversible behaviour :Eq (42) and (58).	K_1	1720.0	J/g
	μ_1	977.0	
	K_2	118.0	
	μ_2	5.8	
	K_3	500.0	
	μ_3	100.0	
	$\varepsilon_c^* = Q_\varepsilon^*$	0.9	(%)
Viscous behaviour : Eq (30) and (46)	$\eta_{c_0} = \eta_{d_0}$	400	KJ.s/g
	$\lambda_e = \lambda_d$	5.10^4	s
	$n_c = n_d$	0.16	-
	$a_c = a_d$	1.20	-
	$K_c = \mu_v$	500.0	J/g

Table B.1 : Coating parameters.

Designation	Parameter	Warp direction	Weft direction	Unit
Time-independant irreversible behaviour : Eq (32) and (35)	G_x	4.0	4.4	KJ/g
	L_x	0.9	0.3	
	H_x	8.0		
	N_x	15.0	35.0	
	M_x	0.1	0.7	
	A_x	12.5	7	-
	ε_x^*	1.4	0.7	(%)
Viscousbehaviour : Eq (29) and (30)	η_{x_0}	$2.9\ 10^3$	$1.6\ 10^3$	MJ.s/g
	λ_x	$42\ 10^3$	$31\ 10^3$	s
	n_x	0.04	0.16	-
	a_x	1.2		-
	K_x	$5.5\ 10^3$		KJ/g
Interaction : Eq (44)	K_γ	60		J/g

Table B.2 : Yarns parameters

References

Alfthan, J. (2004). The effect of humidity cycle amplitude on accelerated tensile creep of paper. Mech. of Time-Dependent Mat., 8: 289-302.

Ambroziak, A. (2006). Application of the Murnaghan model in analysis of non-linear elastic material properties of PVC-coated fabric.Task Quarterly 10 (3): 253-265.

Badel, P., Vidal-Sallé, E., Boisse, P. (2007). Computational determination of in-plane shear mechanical behaviour of textile composite reinforcements. Computational Materials Science 40: 439-448.

Bele, E., Bouwhuis, B. A., Hibbard, G. D. (2009). Microstructural design in work hardenable perforation stretch formed micro-truss cores. Comp. Part A: Appl. Sci. and Manuf., 40: 1158-1166.

Bessert, N., Frederich, O. (2005). Nonlinear airship aeroelasticity. Journal of Fluids and Structures 21:731-742.

Bird R. B., Armstrong R. C., and Hassager. O. (1977) Dynamics of Polymeric Liquids.Wiley,New York.

Bles, G., Nowacki, W.K., Tourabi, A. (2009). Experimental study of the cyclic visco-elasto-plastic behaviour of a polyamide fibre strap. Int. J of Solids and Struc. 46:2693-2705.

Bles, G., Parlier, Y., Leloup, R., Dib, W., Tourabi, A., Leroux, J.-B., Roncin, K., Jochum, C. (2012). High tensile stress on fabrics of giant kites; Beyond-the-sea project. Natural Propulsion Seminar, Marin Institute, Wageningen, Netherlands, 26th january 2012.

Boisse, P., Zouari, B., Daniel, J-L., (2006). Importance of in-plane shear rigidity in finite element analyses of woven fabric composite preforming. Composites: Part A 37 2201–2212.

Bridgens, B.N., Gosling, P.D. (2004). Direct stress-strain representation for coated woven fabrics. Computers and Structures 82: 1913-1927.

Ciortan, C., Guedes Soares, C. (2007). Computational study of sail performance in upwind condition. Ocean Engineering 34: 2198-2206.

Chen,S., Ding,X. (2007). On the anisotropic tensile behaviors of flexible polyvinylchloride-coated fabrics. Textile Research Journal 77 (6):369-374.

Chen,J., Chen, W.,Zhang,D. (2014). Experimental study on uniaxial and biaxial tensile properties of coated fabric for airship envelopes. J. of Reinforced Plastics and Composites33 (7):630-647.

Curnier, A. (2005). Mécanique des solides déformables: Cinématique, dynamique, énergétique (Mechanics of deformable solids : kinematics, dynamics, energetics). PPUR presses polytechniques et universitaires romandes.

Dib, W. (2014). Comportement mécanique de tissus à voile, en fibres synthétiques, sous sollicitations biaxiales et déformation finie (Mechanical constitutive law of a synthetic-fibre woven sailcloth, under biaxial loadings and finite strain). Ph.D. Thesis, University of Grenoble, France.

Dinh, T.D., Rezaei, A., De Laet, L., Mollaert, M., Van Hemelrijck, D., Van Paepegem, W. (2014). A new elasto-plastic material model for coated fabric. Engineering Structures 71: 222-233.

Fitzgerald, J. E. (2008). A tensorial Hencky measure of strain and strain rate for finite deformations. Journal of Applied Physics, 51: 5111-5115.

Fer, F. (1971).Thermodynamique macroscopique 2 (Macrocopic thermodynamics 2). Gordon and Breach science Publishers. New York.

Galliot,C., Luchsinger,R.H. (2009). A simple model describing the non-linear biaxial tensile behavior of PVC-coated polyester fabrics for use in finite element analysis. Composite Structures 90:438-447.

Graf, K., Renzsch, H. (2006). Ranse Investigations of downwind sailsand integration into sailing yacht design processes. 2nd High PerformanceYacht Design Conference, Auckland, 14-16 February 2006.

Horrocks, A.R., Anand, S.C. (Eds.) (2000). Handbook of technical textiles. Elsevier, Woodhead Publishing Limited in association with The Textile Institute.

Kato, S., Yoshino, T., Minami, H. (1999). Formulation of constitutive equations for fabric membranes based on the concept of fabric lattice model. Engineering Structures 21:691-708.

King, M.J., Jearanaisilawong, P., Socrate, S. (2005).A continuum constitutive model for the mechanical behavior of woven fabrics. International Journal of Solids and Structures 42:3867-3896.

Klosowski, P., Komar, W., Woznica, K. (2009). Finite element description of nonlinear viscoelastic behaviour of technical fabric. Construction and Building Materials 23:1133-1140.

Lasher, W. C., Sonnenmeier, J. R. (2008).An analysis of practical RANS simulations for spinnaker aerodynamics. Journal of Wind Engineering and Industrial Aerodynamics 96 :143-165.

Leclère, G., Nême, A., Cognard, J. Y, Berger, F. (2004). Rupture simulation of 3D elastoplastic structures under dynamic loading. Comput.&struct.82 : 2049-2059.

Leloup, R., Roncin, K., Bles, G., Leroux, J.-B., Jochum, C., Parlier, Y. (2013a). Estimation of the Lift-to-Drag Ratio Using the Lifting Line Method: Application to a Leading Edge Inflatable Kite. Airborne Wind Energy, Ed. Ahrens U., Diehl M., Schmehl R., Springer Berlin Heidelberg.

Leloup, R., Roncin, K., Bles, G., Leroux, J.-B., Jochum, C., Parlier, Y. (2013b). A novel modeling for performance assessment of kites as auxiliary propulsion device for merchant ships. 16th International Conference on Computer Applications in Shipbuilding, Busan, South Korea, 2013.

Leloup, R., Roncin, K., Bles, G., Leroux, J.-B., Jochum, C., Parlier, Y. (2014).Kite and classical rig sailing performance comparison on a one design keel boat. Ocean Engineering, 90: 39-48.

Leloup, R., Roncin, K., Behrel, M., Bles, G., Leroux, J.-B., Jochum, C., Parlier, Y. (2016).A continuous and analytical modeling for kites as auxiliary propulsion devoted to merchant ships, including fuel saving estimation. Renewable Energy, 86: 483-496.

Lewis, W.J. (2003). Tension structures, form and behaviour. Thomas Telford Publishing, London.

Le Maitre, O., Souza De Cursi, J. E. and Huberson, S. (1998). Large displacement analysis for ideally flexible sails. Eur. J. Mech. A/ Solids, 17, no4 : 619-636.

Mandel, J. (1974). Introduction à la mécanique des milieux continus déformables (Introduction to deformable continuum mechanics). Série B de Mécanique appliqué (series B of Applied Mechanics). IPPT PAN, Panstwowe Wydawnictwo Naukowe (polish scientific publishers), Warsaw.

Minami, H. (2006). A multi-step linear approximation method for nonlinear analysis of stress and deformation of coated plain-weave fabric. Journal of Textile Engineering 52 (5): 189-195.

Oñate, E., Kröplin, B.-H.(2008). Textile Composites and Inflatable Structures II. Series "Computational Methods in Applied Sciences, Vol. 8", Springer.

Pargana, J.B., Lloyd-Smith, D., Izzuddin, B.A. (2007). Advanced material model for coated fabrics used in tensioned fabric structures. Engineering Structures 29: 1323-1336.

Pargana, J.B., Leitao, V.M.A. (2015). A simplified stress–strain model for coated plain-weave fabrics used in Tensioned Fabric Structures. Engineering Structures 84: 439-450.

Peng, X.Q., Cao, J. (2005). A continuum mechanics-based non-orthogonal constitutive model for woven composite fabrics. Composites Part A 36: 859-874.

Rougée, P. (1997). Mécanique des grandes transformations (Mechanics of finite transformations). Mathématiques & applications (Mathematics & applications), Springer.

Tabiei, A., Jiang, Y. (1999). Woven fabric composite material model with material nonlinearity for nonlinear finite element simulation. International Journal of Solids and Structures36:2757-2771.

Tabiei, A., Yi, W. (2002). Comparative study of predictive methods for woven fabric composite elastic properties. Composite Structures58:149-164.

Wang J., Page J. R., and Paton R.(1998) Experimental investigation of the draping properties of reinforcement fabrics. Composites Science and Technology, 58 :229_237.

Xue, P., Peng, X., Cao, J. (2003). A non-orthogonal constitutive model for characterizing woven composites. Composites Part A 34:183-193.

Yasuda K. (1979). Investigation of the analogies between viscometric and linear viscoelastic properties of Polystyrene fluids. PhD thesis, Massachusetts Institute of Technology, Cambridge (Massachusetts).